JĲM PAPERS

Investigations of shock–boundary layer interaction dynamics using high-bandwidth pressure field imaging

Chase Jenquin[1], Ethan C. Johnson[1] and Venkat Narayanaswamy[1],†

[1]Department of Mechanical and Aerospace Engineering, North Carolina State University, Raleigh, NC 27695, USA

The large-scale pulsations of shock-induced separation with length scale that significantly exceeds the incoming boundary layer thickness are investigated. The shock–boundary layer interaction (SBLI) unit is generated by an inward-turning axisymmetric compression ramp at an inflow Mach number of 2.5. A substantial region surrounding the centre azimuth exhibited mean and dynamic flow features that are consistent with two-dimensional separation. Two-dimensional highly resolved maps of surface pressure field are obtained using fast-response pressure-sensitive paint fluorescence imaging at 40 kHz repetition rate. The measurement domain covered significant regions of the incoming boundary layer through the relaxing boundary layer downstream of the reattachment as well as over 25 boundary layer thicknesses in the azimuthal direction. These measurements provide new insights into the spanwise coupling of the SBLI unit in addition to its inherent dynamics. The power spectral density (PSD) of the centreline pressure exhibits very good agreement with theoretical models and complementary measurements using fast-response pressure transducers, which served to validate the pressure field measurements. Detailed examination of the PSD reveals strong agreement with the literature, which includes the peak Strouhal number of the separation and reattachment shock motions as well as the downward frequency shift along the separation bubble. Furthermore, the pressure fluctuation maps reveal streamwise-elongated structures just downstream of the ramp leading edge that persist well downstream of the reattachment. A time sequence of conditional average pressure fluctuation maps is constructed surrounding isolated pressure excursions in the intermittent region. This sequence, along with two-point cross correlation analysis, provides critical information about the flow processes that drive the separation bubble pulsations in the SBLI units with large separation scales. Overall, the imbalance in the mass within the separation bubble appears to be the critical mechanism that drives

† Email address for correspondence: vnaraya3@ncsu.edu

the separation bubble pulsations. Furthermore, the pressure perturbations originating at azimuthally offset locations are also observed to influence the separation bubble dynamics.

Key words: high-speed flow, shock waves, separated flows

1. Introduction

Shock interactions with boundary layers are persistent and limiting phenomena that cause debilitating outcomes such as premature aerostructure failure due to fatigue and loss of effectiveness of control effects, among others, in high-speed platforms. In internal flows, such as within ramjet and scramjet engines, the shock-induced separation can cause several detrimental phenomena such as high pulsating loading within the engine that results in additional pitching moments, local peaks in heat transfer and even inlet unstart. Clearly, a better understanding of the underlying flow physics can substantially augment the design tools for high-speed aerospace vehicles.

Since first reported by Kistler (1959), the large-scale low-frequency motions of the separation shock continue to be one of the bottleneck phenomena in understanding shock–boundary layer interaction (SBLI) units and has led to substantial research into the governing interactions over the past several decades. These low-frequency motions of the separation shock occur at time scales over two orders of magnitude lower than the boundary layer characteristic frequency, and past research elucidated several sources and mechanisms that drive the separation shock motions. The early works showed that the separation shock motions are indeed driven by separation bubble pulsations and a significant body of literature investigated the sources and mechanisms that drive these separation bubble pulsations. The progress made at different points in time over the past few decades has been summarized in textbooks (Babinsky & Harvey 2011) and review articles (Dolling 1993, 2001; Zheltovodov 2006; Clemens & Narayanaswamy 2014; Gaitonde 2015).

Summarily, previous research has identified broadly two mechanisms that drive the separation bubble pulsations. First is the 'upstream mechanism' where the incoming boundary layer drives the separation bubble. The evidence of the upstream mechanism was reported in intermittent separations as well as modest mean separation scales, wherein the turbulent properties of the incoming boundary layer were correlated with the separation shock motions. Andreopoulos & Muck (1987) were among the first to study the contribution of the incoming boundary layers and they showed that the burst/sweep events of the turbulent boundary layers correlated with the separation shock motions in a compression-ramp-generated SBLI. Later works by Gramann & Dolling (1990) found correlations between the overall incoming boundary layer momentum and the separation shock location of a cylinder SBLI. Subsequently, Erengil & Dolling (1991*a*,*b*) (compression ramp SBLI) and Brusniak & Dolling (1994) (blunt fin SBLI) demonstrated the occurrence of a modest correlation between the pressure fluctuations originating in the incoming boundary layer and the corresponding separation shock location. Beresh, Clemens & Dolling (2002) studied the velocity fluctuations within the incoming boundary layer and showed that the positive (negative) velocity fluctuations in the near-wall region correlated with the separation shock being downstream (upstream); the SBLI unit was once again generated by a compression ramp. Ganapathisubramani, Clemens & Dolling (2006) identified the presence of superstructures that were an order of magnitude longer than the boundary layer thickness in the streamwise direction. Using velocity correlations, Ganapathisubramani, Clemens & Dolling (2009) demonstrated a

direct correlation between the incoming boundary layer momentum fluctuations in the near-wall region and the separation surrogate identified using velocity information. These findings were also in general agreement with those of Humble *et al.* (2009) who used three-dimensional velocity fields to study compression ramp SBLI. A similar observation was also reported by Dussauge & Piponniau (2008) for an incipiently separating SBLI unit generated by an impinging shock. Except for Brusniak & Dolling (1994), all other investigations had a modest separation scale of about twice the boundary layer thickness. More recent exceptions are from Poggie & Porter (2019) and Deshpande & Poggie (2021) who investigated a compression ramp SBLI of a much larger length scale and showed a strong near-wall momentum fluctuation that preceded the separation shock motion by several characteristic boundary layer time scales.

The 'downstream mechanisms' emanate from within the separation bubble, and these mechanisms typically dominate the separation bubble pulsation for large length scales ($L_{sep} > 4\delta$, based on Clemens & Narayanaswamy (2014)). Thomas, Putnam & Chu (1994) studied multiple compression ramp SBLI using pressure fluctuation measurements and suggested that the inherent global instability of the separation bubble causes the pulsations. Pirozzoli, Grasso & Gatski (2004) performed direct numerical simulations of compression ramp SBLI and suggested that acoustic feedback within the subsonic regions of the separation bubble can be a potential driving mechanism. Wu & Martin (2008) performed long-duration direct numerical simulations over a compression ramp SBLI. Unlike Ganapathisubramani *et al.* (2006), Wu & Martin (2008) observed only a modest correlation between the superstructures and the spanwise-average separation surrogate. Instead, they suggested that a wake-type instability of the shear layer can drive the separation bubble pulsations. Touber & Sandham (2009) performed large-eddy simulations on a compression ramp SBLI and demonstrated the existence of a global instability node that amplifies the fluctuations over a range of resonant frequencies. They suggested that the separation bubble can be modelled as a low-pass filter driven by random fluctuations emanating from the turbulent flow. More recent works by Adler & Gaitonde (2018) and Hu, Hickel & Van Oudheusden (2021) considered the SBLI units from a dynamical systems framework.

The role of the shear layer that develops over the separation bubble and the resulting fluid entrainment has been emphasized as a potential driving mechanism by many earlier works. Piponniau *et al.* (2009) developed a phenomenological model based on the eddy growth rate along the shear layer and demonstrated that a new scaling based on the mixing rate models considerably reduced the scatter in the peak separation bubble pulsation frequencies across a variety of Mach numbers ranging from subsonic to supersonic. They suggested that the mass imbalance between the fluid injected into the separation bubble at the reattachment and ejected by the shear layer drives the pulsations; this postulate has been previously suggested by Cherry, Hillier & Latour (1984) and Eaton & Johnston (1981) in subsonic flows and is also in agreement with Priebe & Martín (2012). Shear layer entrainment was also expounded in substantial detail by Estruch-Samper & Chandola (2018) over several large-scale separations generated by a two-dimensional forward-facing step. Their investigations mainly consisted of pressure fluctuation measurements along the streamwise direction, complemented by high-repetition-rate schlieren imaging. Their findings, once again, reiterated the central importance of the entrainment process towards driving the separation bubble pulsations; interestingly, they also point to the indirect contribution of the incoming boundary layer structures towards driving the entrainment.

Recent high-fidelity simulations performed in large separation units revealed several novel insights and entities that can contribute immensely to driving the separation bubble.

The most important among them are the Görtler vortices that were observed by Lüdeke, Radespiel & Schülein (2004) and Loginov, Adams & Zheltovodov (2006) to emanate at the vicinity of the reattachment region; a later work by Zhuang *et al.* (2018) also confirmed their existence experimentally using surface and off-surface imaging of the flow field. While Loginov *et al.* (2006) observed that the Görtler vortices were nearly periodically distributed in the spanwise direction at any given time, Lüdeke *et al.* (2004), Floryan (1991) and Schuelein & Trofimov (2011) noted that the Görtler vortices do not have a fixed originating point at any given time due to the lack of an anchoring mechanism. Pasquariello, Hickel & Adams (2017) observed the Görtler vortices from large-eddy simulation datasets on an impinging SBLI. They further observed that the local presence of the Görtler vortices modified the reattachment locus locally and had a corresponding impact on the separation line. Priebe *et al.* (2016) performed dynamic mode decomposition of a Mach 3 compression ramp SBLI direct numerical simulation dataset and observed that the Görtler vortices formed within the separation bubble and persisted downstream of the reattachment. Their findings also supported the importance of the Görtler vortices within the SBLI unit.

We note that the majority of the experimental investigations (except those of Ganapathisubramani *et al.* (2009) and Humble *et al.* (2009), among others) were performed at a fixed spanwise location (typically model centreline). Similarly, Loginov *et al.* (2006) notes that the limited span of their computational domain (4δ) precluded obtaining further information as to the spanwise organization of the Görtler vortices and suggested that large-span datasets can provide a substantial insight into the underlying mechanics that drive the separated flow motions. However, the computational cost becomes prohibitive for any substantial increase in the domain size while also maintaining high fidelity. This puts a spotlight on the question as to whether some of the underlying mechanisms that drive the separation bubble pulsations are lost by the traditional approaches that fail to capture the influences of regions that are offset in the spanwise direction. In other words, it is possible that the influences of features such as the Görtler vortices extend in the spanwise direction within the separation bubble. If so, then can one potentially reconcile some of the discrepancies present in the literature that are mainly based on restricted span datasets. And more fundamentally, it is important to question if the Görtler vortices and other entities are but a manifestation of a larger underlying phenomenon that occurs within the SBLI unit.

The present study addresses the above questions by demonstrating a two-dimensional pressure field imaged at 40 kHz over a compression ramp SBLI unit. A semicircular inward-turning ramp SBLI was conceptualized to mimic the flow processes in high-speed axisymmetric inlets. The ramp was placed within a semicircular mount to generate the SBLI unit; the mount was again made by truncating a hollow cylinder longitudinally by half. This inward-turning ramp SBLI unit also possessed other desirable features such as large separation scales ($\approx 10\delta$). Despite the SBLI unit being inherently three-dimensional, notable similarities with a two-dimensional SBLI unit were observed over substantial regions surrounding the midspan that allowed comparisons with the two-dimensional SBLI literature. High-repetition-rate pressure maps were obtained across the entire SBLI extending in the streamwise direction about $\approx 15\delta$ within the incoming boundary layer through 4δ into the relaxing boundary layer, and spanwise domain that extended $\pm 12\delta$ about the centreline. The pressure fields were analysed statistically to obtain a holistic understanding of the mean and dynamic coupling with the SBLI unit and elucidate some of the driving mechanisms of the separation bubble pulsations.

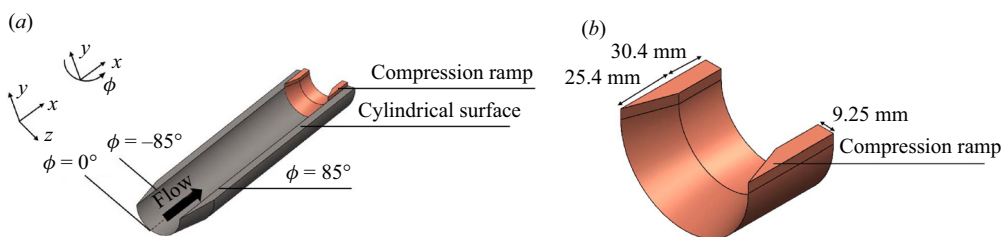| Parameter	Value
M_∞	2.5
u_∞	588 m s^{-1}
T_∞	138 K
Re/m	5.3×10^7 m^{-1}
p_∞	32.5 kPa

Table 1. Free-stream test conditions.

Figure 1. Schematics of the test model: (*a*) assembled view of the compression ramp mounted within the semicircular cylinder surface and (*b*) isometric view of the inward-turning compression ramp. Note that both views represent full test article geometry and not a symmetry view.

2. Experimental set-up

2.1. *Free-stream conditions*

All experiments were performed in the NCSU blowdown supersonic wind tunnel at fixed Mach number of $M_\infty = 2.5$, yielding the free-stream test conditions compiled in table 1. The test section measured 150 mm $\times$ 150 mm $\times$ 650 mm and had optical access from three of its four sides. Each test run was approximately 8 s long and the stagnation pressure was maintained to within 5 % over the test duration. The datasets reported in the present study were obtained over 3.5 s of steady flow operation and over eight runs. The run-to-run repeatability of the stagnation pressure was better than 2 %.

2.2. *Test article and inflow conditions*

The test model consists of a semicircular cylindrical surface made of steel within which an inward-turning steel ramp was installed as shown in figure 1(*a*). The cylindrical surface had a sharp leading edge with an inner diameter of $D = 75$ mm and was placed in the free stream using strut mounts. A fresh boundary layer developed starting at the model leading edge and underwent a natural transition to turbulence. This turbulent boundary layer interacted with the axisymmetric ramp whose leading edge was placed 380 mm downstream of the circular construction leading edge. The compression ramp, shown in figure 1(*b*), had a turning angle of $20°$ and the ramp thickness introduced a maximum constriction of $0.246D$ at its elbow. The open top of the cylindrical surface naturally allows for flow spillage causing the three-dimensionality of the SBLI unit. Table 2 provides greater details of the inviscid pressure ratio and the computed pressure ratio downstream of the inviscid shock computed using Reynolds-averaged Navier–Stokes (RANS) simulations, wherein the additional compression is due to area constriction.

961 A5-5

Parameter	Value
Ramp angle	$20°$
Ramp height	9.25 mm
p_b/p_∞ (two-dimensional)	3.21
p_b/p_∞ (actual)	4.0

Table 2. Compression ramp configuration and planar inviscid/actual interaction pressure ratios.

Parameter	Value
δ	3.5 mm
δ^*	0.26 mm
θ	0.22 mm
H	1.17
Re_θ	11 760

Table 3. Incoming boundary layer characteristics for the half-isolator model.

The boundary layer thickness was measured just upstream of the mean separation location using a single Pitot probe scan with the compression ramp removed during the scans. An earlier work using this same test configuration by Funderburk & Narayanaswamy (2019*a*) reported the boundary layer parameters, and the same parameters were also reproduced in the present study. The boundary layer parameters are presented again in table 3 from Funderburk & Narayanaswamy (2019*a*) for completeness. Summarily, the boundary layer thickness (δ) based on 99 % velocity was determined to be 3.5 mm with $Re_\theta = 11\,760$.

2.3. *Experimental methods*

2.3.1. *Surface streakline visualization*

Surface streakline visualizations were performed to gain a qualitative understanding of the SBLI unit and estimate the separation length scale. The visualization medium consisted of a mixture of mineral oil and a dye pigment that fluoresces red when exposed to UV light, providing excellent contrast against the black model surfaces. The dye mixture is swept by the wall shear, resulting in streakline patterns that qualitatively correspond to the local mean wall shear. In this way, regions of low shear stress (near the separation line, for instance) could be identified through pigment accumulation. Moreover, as the pigment followed the flow over the entire duration of each test, the near-wall streakline trajectories could be deduced in some areas, although only in a mean sense. Plan-view videos of the flow fields were recorded at 60 Hz using a Nikon D5200 DSLR camera, with illumination provided by a 10 W LED UV flashlamp. The field of view was sufficient to image the entire interaction, including the incoming boundary layer and downstream of the reattachment. The streakline visualization images presented in the present work are averaged over 240 frames obtained during four seconds of steady wind tunnel operation.

2.3.2. *Dynamic pressure-sensitive paint measurements*

An in-house-mixed platinum luminophore fast-response polymer/ceramic pressure-sensitive paint (PC-PSP) was employed based on the formulations by McMullen *et al.* (2013). As recommended by the authors, a platinum complex (Pt(II)

meso-tetra(pentafluorophenyl) porphine) was chosen as the luminophore. Two steps were involved in the preparation of the paint. First, a ceramic slurry solution was prepared by mixing distilled water with 12.5 mg of a ceramic dispersant (Rohm & Haas D-3005) per gram of water and 1.25 g of titanium dioxide (TiO_2) per gram of water. After ball-milling the slurry solution for an hour, Rhoplex HA-8 (Rohm & Haas) emulsifier was then added at a weight fraction of 3.5 %. Before the PC-PSP was applied, a commercial base-coat from Innovative Scientific Solutions Inc. (ISSI) was layered on the model surface to prevent rusting. Subsequently, a two-step application of PC-PSP base-coat and the luminophore was made to yield a very smooth finish. The time response of the paint was highly sensitive to paint coat and mixture. The sprayable form of the PSP has been shown to exhibit response times as low as 10 μs for the paint thickness used in the present effort (Egami, Sato & Konishi 2019). The application of the dynamic PSP on curved surfaces has also been demonstrated recently by Leonard & Narayanaswamy (2021), wherein the authors made favourable comparisons of the mean and root-mean-square (r.m.s.) pressures obtained using the PC-PSP and Kulite transducers.

The data reduction from the raw PC-PSP images to pressure fields starts with background subtraction of any residual scattering from the model. This is followed by normalization of the resultant images with a reference 'wind off' image that was obtained at 1 atm and 300 K without the wind tunnel flow. The normalized images are then calibrated using the procedures described in the following sections. Finally, the calibrated pressure fields are binned 3×3 pixels following Varigonda & Narayanaswamy (2021) to provide the best signal-to-noise ratio of the pressure fields without impacting the dynamic content of the pressure field. The resulting spatial resolution of the pressure fields is 0.78 mm per binned pixel.

2.3.3. *Calibration of mean pressure*

Different approaches were used to obtain redundant calibration of the mean pressure from the PC-PSP. The first method was to obtain a Stern–Volmer curve in a pressure- and temperature-controlled optically accessible vacuum oven. The temperature within the oven was set at 295 K, which corresponded to the model surface temperature prior to the test run. The resulting calibration curve did not account for a minor model surface temperature decrease observed during the run; the maximum temperature decrease measured just after the test run was 5 K. Based on the literature on the temperature sensitivity of this paint mixture, the resulting uncertainty of the mean pressure is estimated at 2 %. The second calibration method utilized a commercial PSP (ISSI; model: uniFIB) that had a slow time response, but a much better pressure sensitivity and a considerably lower temperature sensitivity compared to PC-PSP; the uniFIB paint also comes with a manufacturer calibration. The mean pressure field of the SBLI unit was used as a calibration target for the PC-PSP for this method. The third method utilized the mean pressure from high-bandwidth pressure transducers (Kulite Inc.; model: XCQ-062-25A) mounted at discrete points spanning the incoming boundary layer through the ramp leading edge. Overall, all three methods provided excellent agreement with one another, and the maximum discrepancy of the mean pressure was less than 3 % of the local value at any given location.

2.3.4. *Characterization of paint thickness*

For a given paint mixture composition (oxygen mass diffusivity), the thickness of the luminophore coat mainly determines the paint's temporal response. The paint thickness
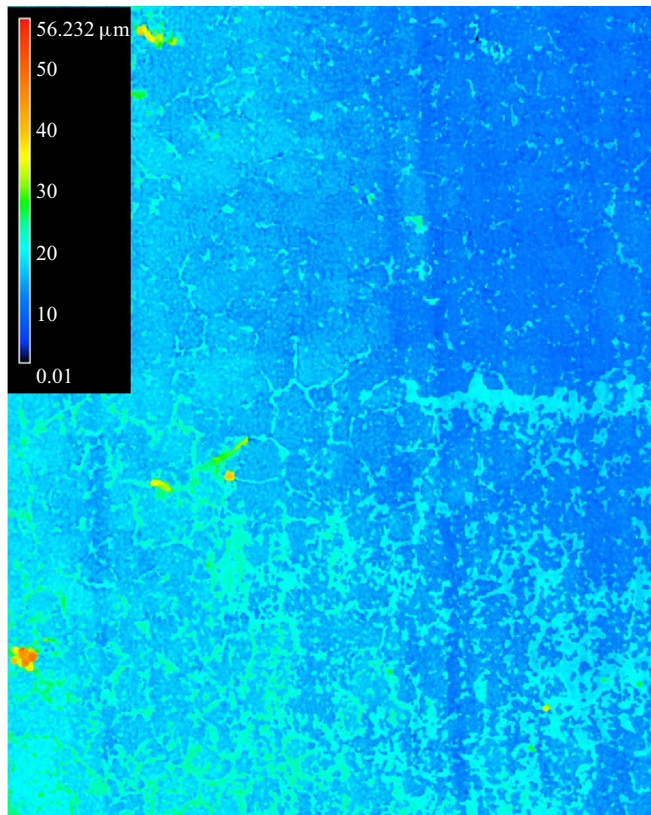
Figure 2. Top-view two-dimensional contour of the measured PSP luminophore thickness over a 1 mm × 1.2 mm region.

was measured with seven luminophore cross-coats that was made in the wind tunnel experiments. The luminophore thickness distribution was quantified over a representative area (1.7 mm × 1.2 mm) using a three-dimensional laser confocal profilometer. For the present study, a flat steel coupon was used and a series of scans with a prescribed overlap were performed and stitched together to generate the map over the desired region of interest. The software provided a two-dimensional array of the measured elevations referenced to an unpainted surface. The mean step height and the r.m.s. were extracted to quantify the paint thickness and surface roughness, respectively. Figure 2 shows a top view of the luminophore layer. It is clear that the paint forms a nearly uniform layer with heterogeneous roughness. The mean height of the luminophore layer was measured at 12.2 μm and the r.m.s. was approximately 1.5 μm. The measurement uncertainty of the device quoted by the manufacturer was 0.05 μm.

2.3.5. *Spectral response of the PC-PSP*

The spectral response of the PC-PSP was computed to determine the signal attenuation and phase shift at different frequencies of interest within the SBLI unit. The approach developed by Winslow, Caroll & Kurdila (2001) was employed and the oxygen mass diffusivity reported in the literature was used. However, recent works show a noticeable disparity in the diffusivities. The spectral response computations based on two extreme values quoted in the literature are presented: $D_m = 1.96 \times 10^{-7}$ m^2 s^{-1} from
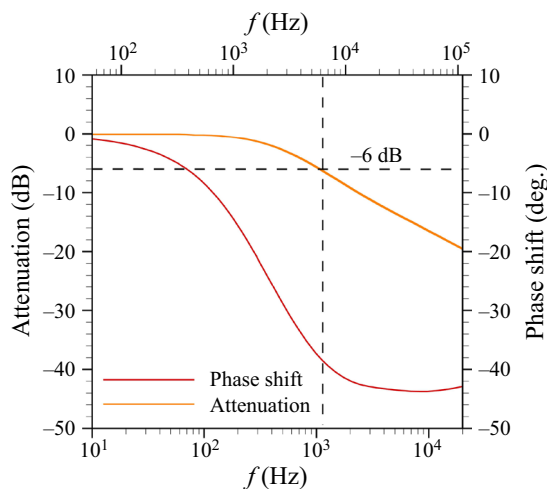
Figure 3. Computed spectral attenuation and phase response of the PSP based on two different diffusivities reported in the literature. The top and bottom x axes represent frequency corresponding to high and low diffusivity.

Kameda *et al.* (2012) and $D_m = 1.1 \times 10^{-6}$ m^2 s^{-1} from Jiao, Peng & Liu (2018). The diffusion time constants through the paint were individually computed with the measured mean paint thickness using the relation $\tau_{diff} = (h^2/D_m)$. The τ_{diff} values were determined as 0.076 and 0.135 ms for the high and low diffusivity values, respectively.

The Bode plot of the paint mixture is presented in figure 3 following the procedure outlined in Funderburk & Narayanaswamy (2019*b*) and other earlier works (Winslow *et al.* 2001; Pandey & Gregory 2016). The Bode plot was generated for a non-dimensional frequency $f \times \tau_{diff}$ and was subsequently scaled to physical frequency units; the frequency units are shown at the top and bottom x axes for 'short' and 'long' diffusion time constants. The spectral attenuation based on the short diffusion time scale shows a nearly zero attenuation for frequencies up to 1 kHz. This is followed by a gradual and subsequently a steep signal attenuation. The -6 dB frequency, which corresponds to 50 % attenuation, occurs at 6 kHz. By contrast, the attenuation for the 'long' diffusion time constant occurs much earlier at around 250 Hz and reaches the -6 dB attenuation at 1.05 kHz. The corresponding phase response curve shows that the phase change between the true and measured value is zero until 100 and 20 Hz short and long diffusion time scales. Some researchers have used a phase shift of $\pi/10$ as a cut-off frequency; this value occurs at 1 kHz and 200 Hz for the short and long diffusion time constants, respectively. The present study has much less of an emphasis on the phase change and a greater emphasis on the overall attenuation as the latter potentially impacts some of the statistics presented. Finally, it is noteworthy that more recent works (Kasai *et al.* 2021) make a substantially greater estimate of the diffusivity (10^{-5} m^2 s^{-1}) that projects a more optimistic paint response; however, this value was not used to generate the Bode plot because of its considerable divergence from other literature values on diffusivity. The strong disparity in the spectral attenuation over the range of diffusivity values considered is resolved in § 3.3.1 by comparing the power spectral density (PSD) of the pressure fluctuations obtained using the PSP and a high-bandwidth pressure transducer.

3. Results and discussion

3.1. *Description of the SBLI unit*

The inward-turning ramp configuration is unusual compared to the literature on the compression ramp SBLI. The intent of employing this configuration is to generate $O(10\delta_0)$ separation scales, which is enabled by the area constriction of the ramp. Funderburk & Narayanaswamy (2019*a*) demonstrated that the area constriction inflates the mean separation scale by two mechanisms. First, the continued flow compression along the ramp face causes a greater back pressure to be presented to the flow due to the coalescence of multiple compression waves along the ramp with the separation shock. This is demonstrated in figure 4(*a*), which presents the pressure field at the centre azimuth in the streamwise/wall-normal plane obtained from RANS calculations of Funderburk & Narayanaswamy (2019*a*); the corresponding value of actual back pressure is also tabulated in table 2. It should be remarked that the predicted separation line from the RANS simulations is 12 % closer to the ramp leading edge compared with the experiments. Hence, the predicted 'actual back pressure' is expected to be underpredicted by a similar extent. In addition to the elevated back pressure, the boundary layer after reattaching to the inward-turning ramp continues to develop under adverse pressure gradient downstream of the reattachment. Funderburk & Narayanaswamy (2019*a*) demonstrated that the adverse pressure gradient downstream of the reattachment causes an additional inflation of the separation scale. Combining these effects with the azimuthal flow relief offered along the edges, the SBLI unit under investigation is three-dimensional by definition.

Now there are two points that need to be emphasized to set this work in the right context with the existing literature. First, the separation bubble of any appreciable size is globally unstable and breaks down into spanwise cellular structures that are inherently three-dimensional. This is illustrated by surface streakline visualizations of different SBLI units (e.g. Loginov *et al.* 2006; Schuelein & Trofimov 2011). Despite the formation of the spanwise cells, the low-frequency motions of the separation bubble were still recorded. Second, in the present work, even though the SBLI unit is inherently three-dimensional, it is demonstrated in the ensuing sections that the magnitude of the spanwise motions in the vicinity of the centre span was small enough that the global mean, r.m.s. and PSD evolution of the SBLI unit share significant quantitative and qualitative commonalities with two-dimensional SBLI units documented in the literature. Certainly, the present SBLI unit is indeed unique and much more complex than a canonical two-dimensional SBLI due to the native extraneous effects present in the SBLI unit. However, despite the extraneous effects, many generalities and similarities occur between the present three-dimensional unit and the canonical two-dimensional SBLI that could be leveraged to yield significant insights that will strengthen our current understanding of both two- and three-dimensional SBLI dynamics.

3.2. *Mean and r.m.s. pressure fields*

The mean and r.m.s. statistics of the pressure fields are first discussed followed by more detailed investigations into the dynamics of the SBLI unit. Corresponding surface streakline visualization fields are also presented to obtain a better understanding of the underlying flow features and mean near-wall flow motions. Obviously, the most direct method to delineate the separation and reattachment lines is using the friction coefficient values and locating the zero crossing locations. This procedure has been routinely followed in computational studies of SBLIs. Unfortunately, obtaining the friction
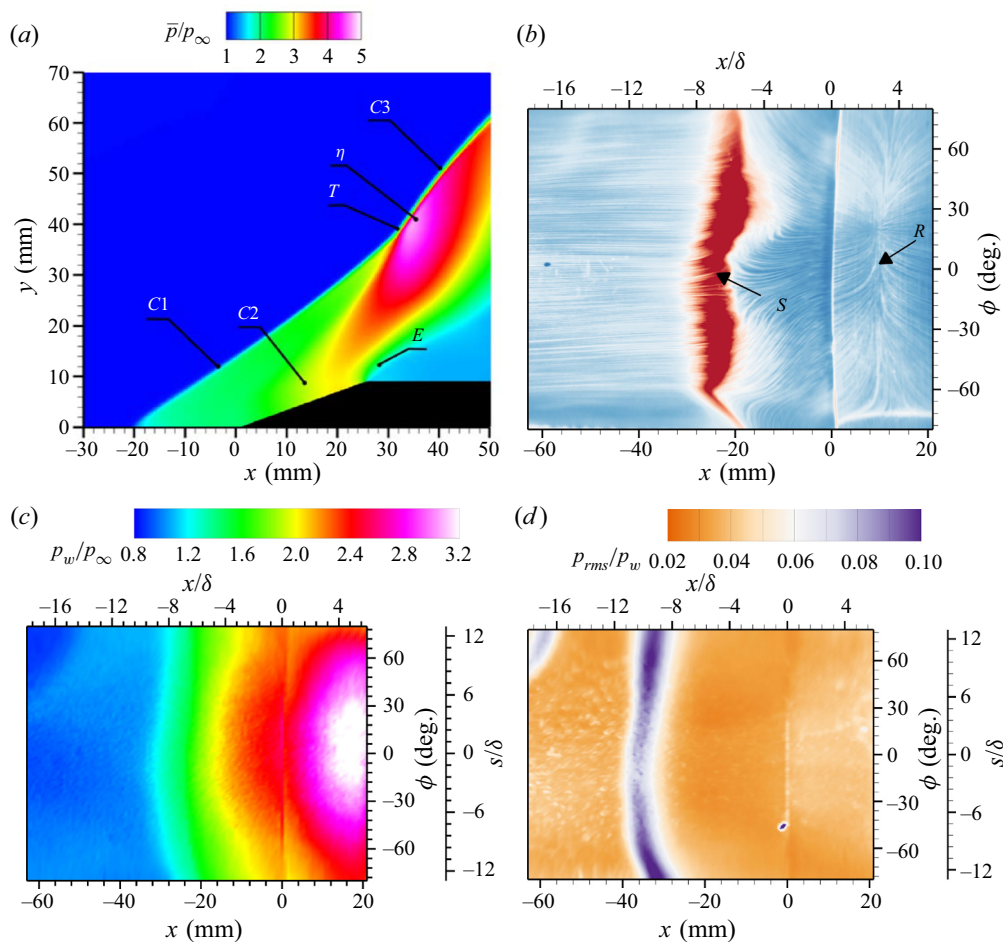
Figure 4. Global description and quantification of the SBLI unit. (*a*) Centre-span pressure field obtained from RANS computations of Funderburk & Narayanaswamy (2019*a*). The labels include the separation shock (C1), the reattachment shock (C2), the inviscid shock (C3), the triple point of separation and reattachment shock coalescence (T), the expansion fan at the ramp shoulder (E) and the elevated compression region (η). Circumferentially unravelled surface streakline and surface pressure fields obtained using PSP: (*b*) ensemble-averaged surface streakline field, (*c*) corresponding mean pressure normalized by free-stream pressure and (*d*) r.m.s. pressure normalized by mean local surface pressure.

coefficient measurements is non-trivial in SBLI units. In this regard, we chose to employ a combination of surface streakline pattern and pressure correlations provided using free interaction theory for making the best estimate of the separation locus. The separation locus from the surface streakline patterns and the free interaction theory agreed with one another within 3 mm (10 % of the separation size). To identify the reattachment locus, we only relied on identifying the nodal points of convergence of streaklines that were very clear in both the ensemble-average surface streakline field as well as tracking the streakline path using the movie of the surface streakline trajectory.

Figure 4(*b–d*) shows the circumferentially unravelled view of the mean and r.m.s. pressure fields along with the surface streakline visualization. The unravelled mean pressure and the surface streakline fields show that the mean upstream influence and separation lines are nearly straight along the circumferential direction in the range $-60° <$

$\phi < +60°$. The average mean separation location over $-60° < \phi < +60°$ is determined to be located at $x_S = -7.3\delta$. Closer inspection of the patterns in the vicinity of the separation line reveals that the circumferential flow motion occurs only beyond $\phi \approx 60°$ and the inclination of the streaklines increases towards the azimuthal direction with increasing ϕ. The surface streakline patterns at the reattachment exhibit at least one identifiable node of streakline convergence and divergence in the range $-30° < \phi < +30°$. Alternating pattern of converging/diverging streaklines has been reported in earlier studies (Loginov *et al.* 2006; Schuelein & Trofimov 2011) and these patterns were found to be associated with high and low mean wall shear stress. Outboard of $\phi \approx \pm30°$, azimuthally outboard motion was observed in the near-wall streaklines in the vicinity of the reattachment line. Interestingly, the alternating converging/diverging patterns no longer appear in this region of azimuthal motions. The mean reattachment location averaged over $-30° < \phi < +30°$ is $x_R = +2.15\delta$. More restrictive choices of azimuths were examined by taking half the azimuthal extent for averaging. However, the resulting change in the mean separation and reattachment locations was between 5 % and 10 %.

Within the separated flow, the mean pressure field (figure 4*c*) exhibits a consistently stronger azimuthal variation with increasing downstream distance. This can be visualized by noting that the mean pressure field in the early parts of separation (-25 mm $\leqslant x \leqslant$ -20 mm) is uniform across the azimuthal direction, while the pressure contours further downstream extend over increasing number of colour bands along the azimuthal direction. It is important to note that the azimuthal extent corresponding to greater than $0.9 \times p_w$ still covers the region $-50° < \phi < +50°$ ($\approx \pm 8\delta$) in the reattachment region. The trends of increasing spanwise pressure variation with downstream distance can be understood by noting that the static pressure just downstream of the separation line is only slightly higher than the free-stream pressure at the edges of the test article. However, the corresponding mean pressure in the downstream regions of the separated flow continuously increases with distance. The azimuthal edges of the ramp/mount maintain their pressure close to the free-stream pressure as observed in the mean pressure field. This pressure differential between the SBLI unit and the azimuthal edges causes a azimuthal pressure gradient between the centre regions of the SBLI and the azimuthal boundaries, and this gradient increases with downstream distance along the SBLI.

The p_{rms}/p_w field presented in figure 4(*d*) exhibits a low value in the incoming boundary layer that is followed by a sharp increase in the intermittent region ($x = -9.6\delta$). This peak is followed by a plateau within the separated flow that extends until the compression ramp leading edge. A moderate increase in p_{rms}/p_w is observed downstream of the ramp leading edge in the vicinity of the reattachment line and reaches a broad peak at the reattachment line. All these features are also observed in a two-dimensional SBLI unit generated by compression ramps and impinging shocks. A differentiating feature of the present unit is the continued increase in p_{rms}/p_w downstream of the reattachment line. We posit that this continued increase can be because the flow field downstream of the reattachment develops along a converging passage that is accompanied by an adverse pressure gradient. The characteristic (integral) frequency of the boundary layer scales as U_e/δ_0, where U_e is the boundary layer edge velocity and δ_0 is the local boundary layer thickness. In a decelerating flow, the edge velocity decreases with downstream distance. As a result, the dominant (characteristic) frequency of the pressure fluctuations also decreases with downstream distance. Because of this decrease, increasingly larger spectral band of unsteadiness is captured by the PSP that results in the downstream p_{rms}/p_w increase.

The elevated p_{rms}/p_w contours in the intermittent region appear straight along the circumferential direction suggesting a nearly two-dimensional separation shock front that
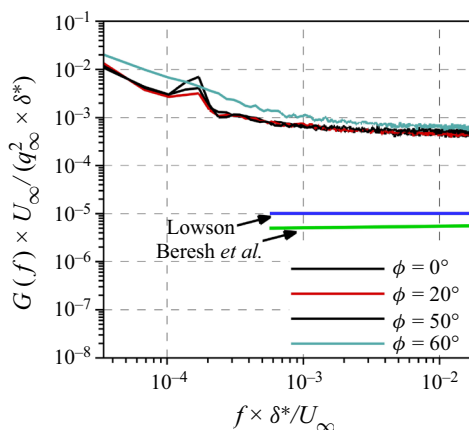
Figure 5. Comparison of wall pressure fluctuation PSD obtained beneath the incoming boundary layer at different azimuthal locations. Comparisons with previous measurements from Beresh *et al.* (2011) and the empirical predictions of Lowson (1968) are also presented.

was also observed in the separation locus of streakline visualization and mean pressure fields. Whereas the magnitude of p_{rms}/p_w is constant in the range $-30° < \phi < +30°$ ($s \approx \pm 6\delta$), it can be observed to increase by up to 20 % at $\phi = +45°$ and continues to stay above the centreline value even at considerably outboard locations. This propounds a potential link between the circumferential flow motion and the elevation of p_{rms}/p_w. The magnitude of p_{rms}/p_w in the reattachment region is also constant in the range $-50° < \phi < +50°$ and decreases at azimuthally outboard locations. Overall, both mean and r.m.s. pressure fields and mean surface streakline patterns show that the SBLI exhibits a two-dimensional nature over a circumferential region ($s \approx \pm 6\delta$), which is sufficiently large to make detailed measurements in this flow unit.

3.3. *Dynamics of pressure fluctuations*

3.3.1. *Power spectral density*

The PSD of the surface pressure fluctuation was computed over the entire measurement domain to characterize both the streamwise and spanwise variations of the surface pressure dynamics caused by the three-dimensional flow motions. Figure 5 shows the PSD of the incoming boundary layer over different azimuthal locations. The coordinates are normalized to compare the PSD with the literature. Figure 5 shows that the PSDs across all the azimuthal locations are nearly identical, evidencing the two-dimensional nature of the inflow boundary layer. The PSD exhibits a decay at very low frequencies followed by a plateau for non-dimensional frequencies greater than 10^{-3}.

The empirical curve fit of Lowson (1968) also predicts a PSD plateau at very low non-dimensional frequencies and the predicted PSD magnitude by the curve fit is presented in figure 5 along with the more recent measurements of a Mach 2.5 boundary layer PSD by Beresh *et al.* (2011). Comparing the plateau with the literature shows that the measured plateau is over an order of magnitude higher than the curve fit of Lowson (1968) and Beresh *et al.* (2011). One possibility is that the value of the displacement thickness δ^* in the normalization was estimated as 1/8 of the boundary layer thickness (δ) as suggested by Lowson based on incompressible boundary layer datasets; typically, δ^* of the compressible boundary layers are a higher fraction of δ.
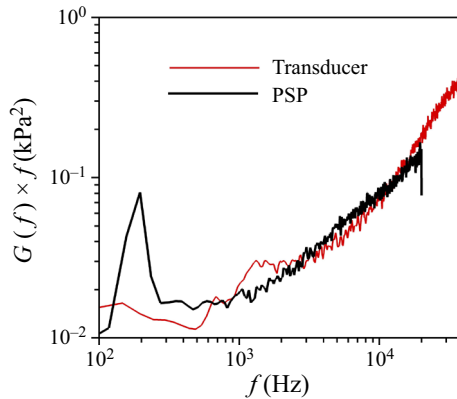
Figure 6. Direct comparison of the frequency-premultiplied wall pressure fluctuation PSD obtained using PSP and pressure transducer beneath the incoming boundary layer, measured at the same location.

Another possibility for the discrepancy is that the noise floor of the PSD becomes dominant and the plateau that is obtained in figure 5 is simply the noise floor. To evaluate this possibility, wall pressure measurements were obtained using Kulite transducers within the incoming boundary layer. Figure 6 shows the comparison between the frequency-premultiplied PSD of the pressure fluctuations obtained from the PSP and Kulite transducers; physical units are retained in figure 6 to make a direct comparison. It can be observed the measured PSDs from both PSP and transducers agree very well with one another over the entire frequency range that could be resolved. A noticeable difference is the spike in the PSD from the PSP method at 200 Hz. This spike pervades the PSD across the entire measurement domain, and it does not correspond to a physical value, as seen from its absence in the Kulite measurements. In the remaining sections, the spike is ignored in the discussions that accompany the PSD. It should also be noted that the incoming boundary layer poses the greatest limitation on the dynamic pressure measurements using PSP within a SBLI unit because of the very small pressure fluctuations in the incoming boundary layer, as shown by Funderburk & Narayanaswamy (2019b). The fact that there is a very good agreement between the PSP- and transducer-based PSD measurement provides enough confidence about the accuracy of the PSD in other locations of the SBLI units that is presented subsequently.

The corresponding frequency-premultiplied pressure fluctuation PSDs within the separation bubble obtained at $x = -11.6$ mm ($x \approx -3\delta$) are presented across different azimuthal locations in figure 7(a). The PSD exhibits a monotonically increasing trend with frequency, which suggests that the peak of the PSD occurs above the frequency range that could be measured by the PSP. It should be noted that there is indeed a significant low-frequency content in the separation bubble PSD as was observed in earlier works (e.g. Pasquariello *et al.* 2017). The reason why the low-frequency content is not emphasized in figure 7(a) is because the plots are frequency-premultiplied PSD. We note that it is possible that the low-frequency content is too weak in the frequency-premultiplied PSD such that the current measurements cannot capture the peak. Between the different azimuthal locations, the PSDs are nearly identical to one another. The overall spread in the PSD between $\phi = 0°$ and $\phi = -45°$ never exceeded 20 % within the measured frequency range, which demonstrates a consistent evolution of the shear layer over the separation bubble along the azimuthal direction.
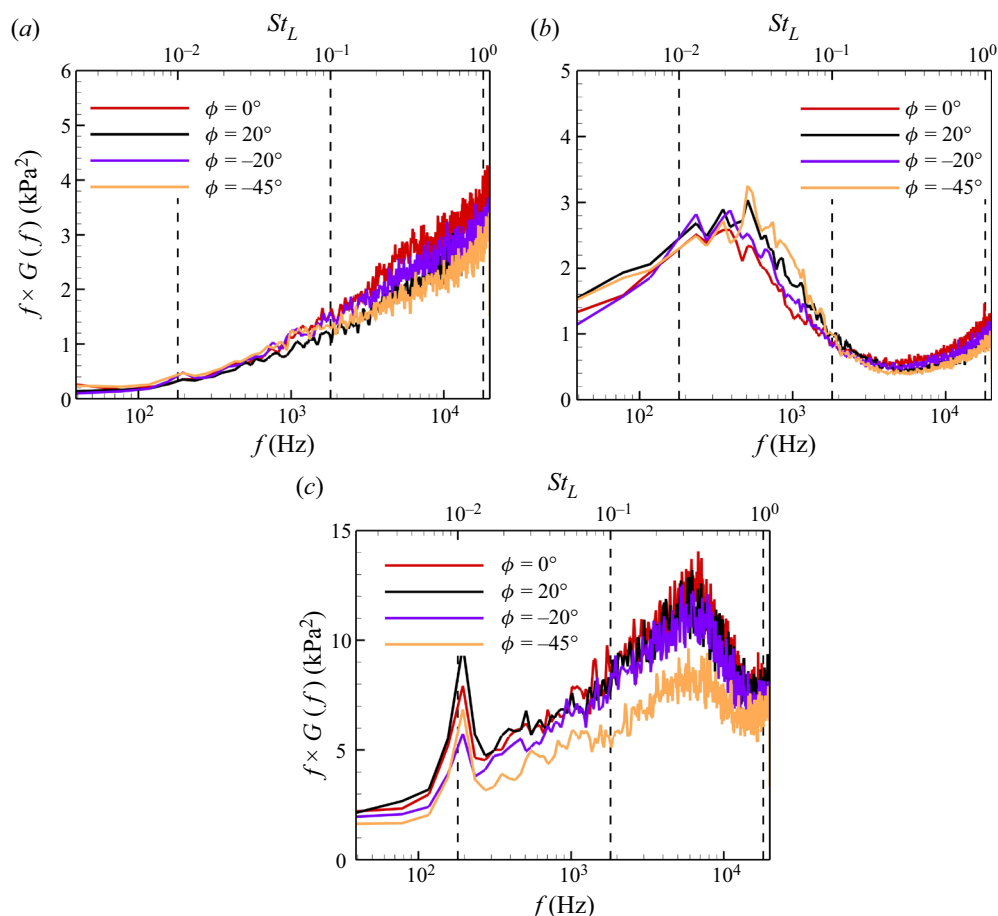
961 A5-14

Figure 7. Frequency-premultiplied wall pressure fluctuation PSD obtained at characteristic locations within the SBLI unit over different azimuthal locations: (*a*) separation bubble ($x \approx -3\delta$), (*b*) intermittent region ($x \approx -9.5\delta$) and (*c*) reattachment location ($x \approx +2.1\delta$).

The intermittent-region PSDs, obtained at $x = -8.5\delta$, are presented in figure 7(*b*) to determine how the separation shock pulsations vary in the azimuthal direction. Both physical frequency unit and a Strouhal number scale based on the spanwise-average separation length are presented. The PSDs in the vicinity of the azimuthal centre exhibit a broadband peak at 350 Hz ($St_L = 0.0193$) and the broadband PSD reaches a minimum at 4 kHz ($St_L \approx 0.24$). These peak Strouhal numbers are within the range of $St_L = 0.02 \pm 0.01$ reported in Dolling (1993) and Dupont *et al.* (2005) who collected multiple experimental works on unswept and swept compression ramp interactions and impinging shock interactions. The minimum in the PSD is followed by another elevation in the PSD that extends until (and beyond) the maximum frequency that could be measured. This elevation is likely caused by the passage of the boundary layer structures that causes jitter motions in separation shock, as suggested by Erengil & Dolling (1991*b*). Overall, the PSDs were very consistent between $\phi = 0°$ and $\phi = -45°$ and the maximum shift in the peak St_L did not exceed 50 Hz ($\Delta St_L \approx 0.0025$).

The pressure PSDs of the reattachment region that capture the dynamics of reattachment shock, obtained at $x = +2.1\delta$, are presented in figure 7(*c*). The PSDs in this region exhibit
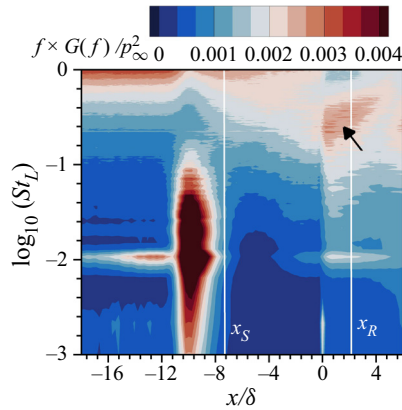
Figure 8. Streamwise evolution of frequency-premultiplied pressure fluctuation PSD obtained at $\phi = 0°$. The abrupt occurrence of the PSD elevation at $St_L \approx 0.2$–0.4 is indicated by an arrow.

a monotonically increasing PSD with frequency with a broad hump at 7 kHz ($St_L \approx 0.4$). The overall magnitude of the PSD is noticeably higher than the intermittent-region PSD, which is caused by the elevated pressures in the reattachment region. Furthermore, the peak Strouhal number of the reattachment-region PSD is approximately 20 times higher than the intermittent-region peak Strouhal number. This ratio is similar to the value quoted by Estruch-Samper & Chandola (2018) ($\approx 33\times$) on a forward-facing step SBLI. The reattachment-region PSD also exhibits excellent agreement over the different azimuthal locations presented. The greatest difference occurs at $\phi = -45°$, where the PSD is lower by about 40 % compared with that at $\phi = 0°$. This reduction is believed to be caused by a combination of azimuthal flow motions and the mean azimuthal undulations in the reattachment region that were also noticed in the surface streakline patterns (figure 4b).

3.3.2. *Streamwise evolution of the PSD*

The streamwise evolution of the frequency-premultiplied pressure fluctuation PSD is presented along $\phi = 0°$ in figure 8. The incoming boundary layer is captured over an extent of 7.5δ ($-18\delta \leqslant x \leqslant -10.5\delta$) and the PSD contours show nearly horizontal colour bands along the streamwise direction. These horizontal bands show that the PSD is essentially identical and maintains the same peak frequency, which was not resolved in the measurements. The intermittent region is seen as the region of elevated PSD in the low-frequency bands over $-10.5\delta \leqslant x \leqslant -8.0\delta$. The length scale of the presence of the low-frequency bands can provide another measure of the length scale of shock motion; this is determined to be 10 mm (2.5δ or $0.3 \times L_{sep}$). Together with the peak Strouhal number of 0.019, the characteristic shock velocity is estimated at 7.4 m s^{-1} or 1.2 % of the free-stream velocity. This estimate is lower than the typical 2 % that is reported in the literature; however, lowering of the separation shock velocity with increasing separation size is consistent with Estruch-Samper & Chandola (2018).

Within the separation bubble, the PSD shows that the individual colour bands show a linear downward tilt in frequency with downstream distance. Noting that p_{rms}/p_w remains constant along the separation bubble and invoking the self-similar nature of the frequency-multiplied PSD within the separation bubble reported by Estruch-Samper & Chandola (2018), this downward tilt in the PSD bands shows a downward shift of the peak

961 A5-16

frequency with downstream distance along the separation bubble. Furthermore, noting that the pressure fluctuations within the separation bubble are predominantly caused by the shear layer above the separation bubble, the shift in the peak frequency demonstrates the growth of the characteristic eddy length scale with downstream distance. These findings have been documented in the literature for different shock-induced separation units. It should be commented that our pressure fluctuation PSD does not resolve the peak frequency of the separation bubble from its inception downstream of the separation shock until the ramp leading edge.

For the compression ramp interactions, the available experimental data on peak frequency extend only until the ramp leading edge because of the difficulty with incorporating the transducers on the compression ramp. In this regard, the present work provides a new insight into the pressure dynamics downstream of the compression corner. Figure 8 shows that a new band of PSD elevation in the Strouhal number range $St_L = 0.2$–0.4 occurs just downstream of the compression ramp leading edge (indicated by an arrow). This new band occurs rather abruptly and sharply departs from the linearly decreasing trend of the peak Strouhal number of the separation bubble PSD that occurred until the ramp leading edge. Downstream of the ramp leading edge, the $St_L = 0.2$–0.4 band maintains its strength but shifts to slightly higher frequency until mean reattachment; the strength of the band quickly dissipates downstream of the reattachment. It should be noted that the relaxing boundary layer has not recovered to a canonical boundary layer PSD until the ramp elbow located 3.5δ downstream of the mean reattachment line.

A similar abrupt appearance of the $St_L = 0.2$–0.4 band was also observed downstream of the compression corner in large-eddy simulations of Grilli *et al.* (2012) as well as in an impinging SBLI configuration downstream of the theoretical incident shock impingement location reported by Pasquariello *et al.* (2017). This, however, contradicts the observations made in the forward-facing step configuration by Estruch-Samper & Chandola (2018) where the authors did not report a separate band of frequencies that is well below the shear layer frequency. More discussions on the distinguishing flow features are presented in the subsequent sections. Overall, the PSD evolution along the SBLI unit shows excellent commonalities with two-dimensional SBLI units and provides experimental support for the abrupt occurrence of the $St_L = 0.2$–0.4 band in the reattachment region that was discovered earlier by Grilli *et al.* (2012) and Pasquariello *et al.* (2017) in two-dimensional SBLI units.

3.4. *Spatiotemporal organization of pressure fluctuations*

Pressure fluctuation fields were extracted from the instantaneous pressure fields and analysed to discern their spatial organization at different regions of the SBLI. Figure 9(*a–i*) shows a representative sequence of nine pressure fluctuation fields spanning 1 ms starting from an overall zero pressure fluctuation (p'/p_∞) in the intermittent region (separation shock at its mean location). One in every five frames are presented (0.125 ms between successive frames) and the entire sequence is shown in supplementary movie 1 available at https://doi.org/10.1017/jfm.2023.168. In each panel, the streamwise-averaged location of the pressure isocontour corresponding to $p/p_\infty = 1.2$, averaged over $\phi = \pm 20°$, is shown as a white dashed line to mark the mean streamwise location of surrogate separation shock; the choice of $p/p_\infty = 1.2$ to mark the separation shock is because of its close correspondence with the peak of p_{rms}/p_w and also follows the recommendation of Poggie & Porter (2019). The instantaneous $p/p_\infty = 1.2$ isocontour for a given realization is shown in each panel to delineate the location of the separation shock at each instant. There are
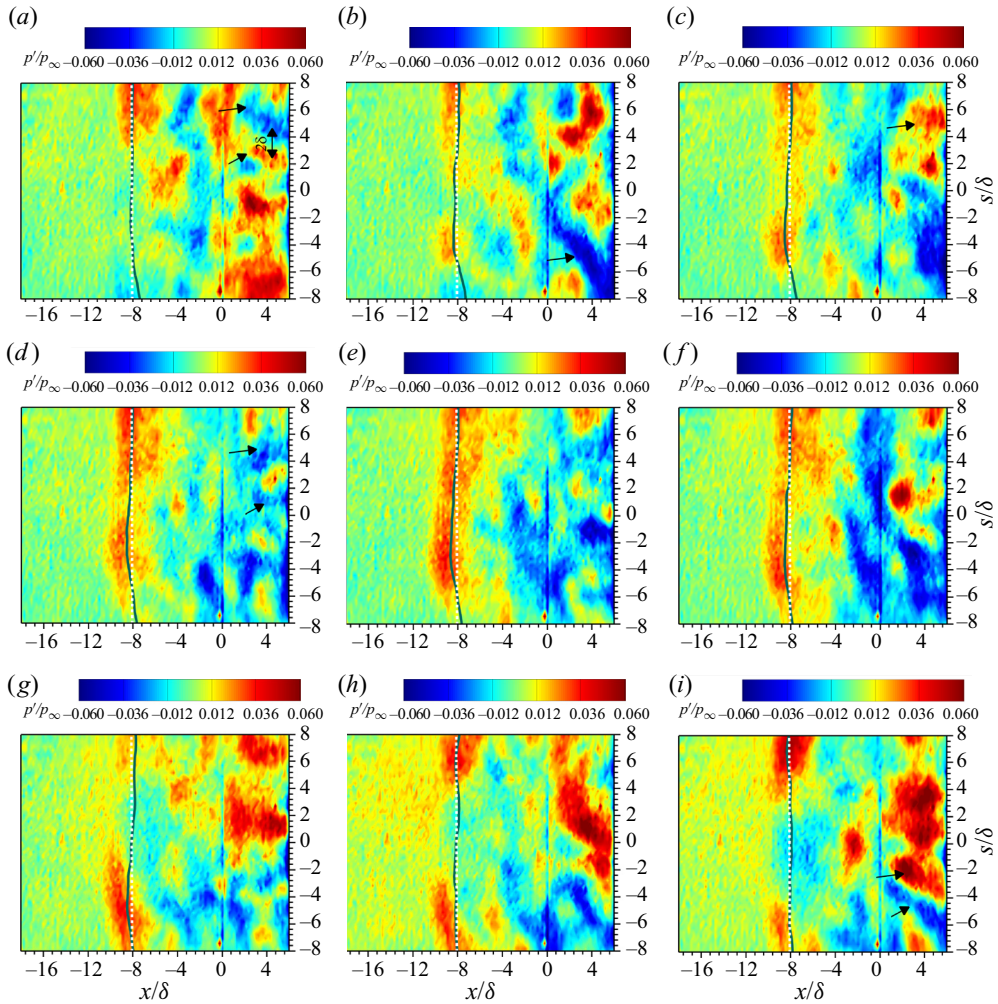
Figure 9. Time sequence of surface pressure fluctuation field, normalized by the free-stream pressure, within the SBLI unit over a duration of 1 ms: (*a*) $t = 0$ ms, (*b*) $t = 0.125$ ms, (*c*) $t = 0.25$ ms, (*d*) $t = 0.375$ ms, (*e*) $t = 0.5$ ms, (*f*) $t = 0.625$ ms, (*g*) $t = 0.75$ ms, (*h*) $t = 0.875$ ms and (*i*) $t = 1$ ms. The red and blue contours correspond to positive and negative pressure fluctuations, respectively.

no similar thresholds available for reattachment shock and hence the reattachment shock location is not marked.

Starting with the intermittent region, we note that the positive and negative pressure fluctuations in this region would correspond to the separation shock instantaneously located upstream and downstream of the mean location, respectively. At $t = 0$ ms, the intermittent region exhibits an overall zero fluctuation for almost the entire domain except $s > 4\delta$, where a positive pressure fluctuation region can be observed. Over the next 0.5 ms, this positive pressure fluctuation band has engulfed the entire intermittent region, as observed in figure 9(*e*). In fact, figure 9(*a–e*) shows two disparate regions of positive pressure fluctuations occurring in the intermittent region at different azimuthal locations and merging with one another to engulf the entire azimuthal extent of the intermittent region by $t = 0.5$ ms. At $t = 0.75$ ms, a break is seen in

961 A5-18

the positive pressure fluctuation band in the range $-1\delta < s < +4\delta$. By $t = 1$ ms, a weak negative pressure fluctuation can be observed in this region in figure 9(*i*). Beyond $t = 1$ ms, this negative pressure region grows in strength and extent, and the next positive pressure fluctuation cycle sets in subsequently. It should be noted that the extent of the positive/negative region during a given cycle does not occupy the entire azimuthal region for most of the cycles. Both positive and negative pressure fluctuations coexist over most of the cycles and compete with one another for space and strength.

The pressure fluctuations in the separated flow region, presented in the sequence of figure 9, exhibit spotty or spanwise-elongated organization until upstream of the ramp leading edge ($x/\delta = 0$). Many such spots of positive and negative pressure fluctuations can be observed in figure 9(*a–d,g–i*) while figure 9(*e,f*) exhibits certain regions where the pressure fluctuations are elongated in the spanwise direction. Upon closer observation, the positive pressure fluctuation in the intermittent region (separation shock upstream) is broadly accompanied by a negative pressure fluctuation in the separation region especially near the ramp leading edge ($x > -4\delta$; figure 9*e,f*). In fact, this correspondence occurs at a local level (at a given azimuth) – i.e. a positive (negative) pressure fluctuation band in the intermittent region at a given azimuthal location is accompanied by a negative (positive) pressure fluctuation band in the separation bubble in the vicinity of the ramp leading edge at the same azimuthal location (see figure 9*h,i*). Interestingly, the separation region close to the intermittent region, where the shear layer is in its initial growth phase, does not exhibit these correlated pressure fluctuations with the intermittent region.

The pressure fluctuation structures downstream of the ramp leading edge appear to get elongated in the streamwise directions in many instances to form streaks of pressure fluctuations in the reattachment region and the downstream relaxing boundary layer. This can be observed in figure 9(*a,c,d*) where black arrows indicate the elongated structures. Whereas these streaks are oriented along the streamwise direction in several instances (e.g. figure 9*a,c,d* indicated by arrows), they get tilted in the azimuthally outward direction in many other instances (e.g. figure 9*b,i* indicated by arrows). Interestingly, the tilted structures occur predominantly in the azimuthal outboard locations, which suggests that the tilting is caused by strong spanwise flow migration at the outboard locations. It should be noted that the streamwise-oriented streaks did not have any preferred azimuthal location. Successive streaks are typically spaced between 2δ and 4δ; one such spacing is labelled in figure 9(*a*). Furthermore, the streamwise-oriented streaks extended over the entire azimuthal domain in many realizations (e.g. figure 9*a,d*). The latter was one of the observations that was sought by Grilli, Hickel & Adams (2013) where the limited spanwise extent of their computational domain (4δ) precluded making predictions of the periodicity or prevalence of the streamwise-elongated structures over larger spanwise domains. The streamwise-elongated streaks in the relaxing boundary layer were not organized as positive and negative fluctuation structures in contrast to the incoming boundary layers, where Ganapathisubramani *et al.* (2006) showed the alternate occurrence of streamwise-elongated positive and negative momentum fluctuation structures. Instead, figure 9 reveals that the sign (positive or negative) of the pressure fluctuation downstream of the ramp leading edge broadly correlates to the inverse sign of the intermittent-region pressure fluctuation along the same azimuth. As a result of the strong variations in the pressure fluctuations, the isocontours of p/p_∞ are a lot more undulatory in the reattachment region compared with the intermittent region; this undulatory pattern was also observed in the coefficient friction maps of two-dimensional SBLI by Priebe &

Martín (2012). It should be noted that at the instances when the streamwise-elongated streaks of pressure fluctuations did not occur in the reattachment region, the pressure fluctuation structures were largely patchy in appearance (e.g. red contours of figure 9*b*,*f*).

Coming to the incoming boundary layer, we note that the measurement technique is not sensitive enough to the delineate any patterns or structures of the pressure fluctuation field within the incoming boundary layer. As such, any existing correlation between the incoming boundary layer pressure fluctuations and those within the SBLI is not evident from the sequence. A more detailed two-point correlation analysis is subsequently presented to elucidate the statistical correlations that exist between the boundary layer and the SBLI pressure fluctuations.

In the light of the above observations, it is likely that the streamwise-elongated pressure fluctuation streaks observed are caused by the passage of streamwise vortices which are generated just in the vicinity of the compression corner. The RANS simulations by Funderburk & Narayanaswamy (2019*a*) showed that this region surrounding the compression corner has the maximum flow turning curvature, which is also consistent with the observation made by Priebe *et al.* (2016). Priebe *et al.* (2016) further demonstrate that the Görtler number exceeded the critical value within the separation region, and this resulted in streamwise-oriented Görtler vortices that propagate downstream through the SBLI unit and beyond. Unfortunately, for the present work, only a lower-bound estimate of the Görtler number could be made since we do not have an experimental value of the radius of curvature (R), and have to base our estimate on the RANS calculations. With this caveat, the RANS calculations (presented in Funderburk & Narayanaswamy 2019*a*) in the vicinity of the compression corner estimated $R \approx 50$ mm ($\approx 14\delta$), which is very similar to estimates of Priebe *et al.* (2016). A similar procedure was also adopted by Hu *et al.* (2021) where the authors computed the Görtler number along the streamwise direction at two different wall-normal distances and reported very similar values between them. With this estimate of the radius of curvature, the corresponding value of the Görtler number is 3.15, which exceeds the critical value presented by Smits & Dussauge (2006) for both laminar flow ($Gt = 0.6$) as well as turbulent separated flow ($Gt = 0.03$ is a generally accepted value) by a considerable margin. Thus, it is likely that the streamwise streaks that emanated in the vicinity of the compression corner are possibly the footprints of the streamwise vortices from Görtler instability. Connecting the power spectra just downstream of the ramp leading edge and the sudden occurrence of the streamwise streaks, we posit that these streaks are responsible for the $St_L \approx 0.2$–0.4 band downstream of the ramp leading edge. It should be remarked that the reattachment PSD shown in figure 7(*c*) captures the motions of the reattachment shock, which has a broadband spectrum with peak frequency at $St_L \approx 0.4$. However, figure 8 shows that the $St_L \approx 0.2$–0.4 band possibly caused by the streamwise streaks occurs upstream of the reattachment region and continues to persist through the reattachment region. This continued evolution of the $St_L \approx 0.2$–0.4 band downstream of the compression corner suggests that the motions of the reattachment shock are indeed influenced (or possibly driven) by the streamwise-oriented structures that emanate at the compression corner. In other words, the reattachment shock dynamics and the passage of the streamwise vortices through the reattachment region are intimately connected with one another. This inference is also supported by earlier computational investigations of Pasquariello *et al.* (2017), Grilli *et al.* (2012) and Priebe *et al.* (2016), among others. Thus, the PSD of reattachment shock motions and the PSD signature that is thought to emerge from the streamwise vortices cannot be distinguished from one another in figures 7(*c*) and 8.
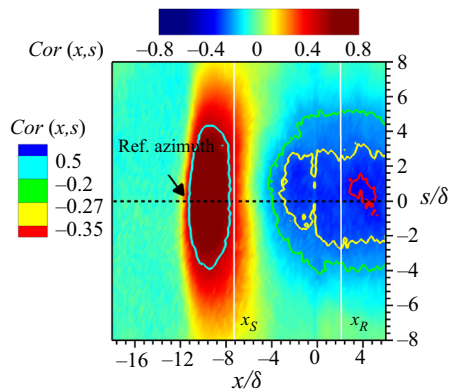
Figure 10. Two-dimensional contour of the zero time lag cross-correlation across the SBLI unit with the intermittent region as the reference location.

Several questions arise at this point:

(i) Is there any relationship between the streamwise vortices in the reattachment region and the separation shock motions?

(ii) Do the pressure fluctuations in the relaxing boundary layer downstream of the reattachment region impact the separation shock motions?

(iii) What is the role, if any, of the incoming boundary layer in the SBLI dynamics?

3.4.1. *Zero time lag cross-correlation and cross-coherence mapping*

Zero time lag cross-correlation analysis was performed to determine the regions of the SBLI whose pressure fluctuations have appreciable positive or negative correlations with the reference location, chosen as the intermittent-region peak p_{rms}/p_w location $x = -8.5\delta$ at $\phi = 0°$. This reference location is also maintained for the subsequent analysis. Figure 10 shows the contour of the zero time lag cross-correlation ($Cor(x, s)$) capturing both streamwise and azimuthal domains. A few select isocontour traces are included to emphasize the topology of the correlated region. It can be observed that the pressure fluctuations within the intermittent region exhibit very low correlation with the incoming boundary layer. This low correlation is expected with large separation sizes, wherein the separation shock is minimally impacted directly by the incoming boundary layer momentum fluctuations as stated by Clemens & Narayanaswamy (2014) and others. Stepping into the intermittent region, figure 10 shows a region of positive correlation surrounding the reference location that stretches across $s = \pm 8\delta$; the extent of $Cor(x, s) > 0.5$ extends between $s \approx \pm 4\delta$. The streamwise extent of the region of $Cor(x, s) > 0.5$ is approximately 2.5δ, which is similar to the intermittent-region length obtained from p_{rms}/p_w values.

Within the separated flow, a narrow passage of very low correlation can be observed in the early portions of the separated flow corresponding to where the shear layer is in its initial growth phase. Further downstream into the separated flow, appreciable negative correlation emerges, and the occurrence of the negative correlation statistically affirms the similar observation made with the instantaneous snapshots of the pressure fluctuations made in the earlier section. The negative correlation intensifies with downstream distance well into the reattachment region and the relaxing boundary layer. In fact, the highest negative correlation occurs within the relaxing boundary layer just downstream of the

mean reattachment. This peak negative correlation location still lies more than 3δ upstream of the ramp shoulder where the expansion process can impact the correlations (Loginov *et al.* 2006). Figure 10 shows that the region of negative correlation ($Cor(x, y) < -0.2$) in the separated flow and downstream is spread over a wide azimuthal region ($-4\delta < s < +4\delta$) even though the highest negative correlation is confined to a small spread of azimuth.

Overall, the zero delay correlations provide very interesting pointers to the different interactions that potentially occur in the SBLI units investigated. First and foremost, the regions within the separation unit that are most correlated with the intermittent region occur near the ramp leading edge, reattachment region and just downstream. Second, the streamwise-elongated topology of the regions of high negative correlation indicate a potential role of the streamwise vortices that emanate in the vicinity of the reattachment and convected along the relaxing boundary layer. Such a role and accompanying mechanism of these Görtler-like vortices were also suggested by earlier researchers and the differences between those works and the current findings are elaborated in § 4. Third, the azimuthal spread of the negatively correlated regions shows that the separation shock at a given location is impacted by the events that occur over a significant azimuthal distance within the separated flow, reattachment region and the relaxing boundary layer. Juxtaposing this comment with the large azimuthal spread of the positively correlated region within the intermittent region raises two possible scenarios for how the pressure fluctuations within the reattachment region can influence the separation shock: (1) the pressure fluctuations originating at an azimuthally distanced location in the separated flow diffuse through the separation region and reach the reference location and/or (2) the pressure fluctuation originating at an azimuthally distanced location in the reattachment region impacts a different azimuthal location in the intermittent region, which then propagates in the azimuthal direction to the reference location. The flow processes that lead to these scenarios are nonlinear and are addressed in the subsequent sections.

Before the impact of the different possible regions on the separation shock dynamics is explored further, it is essential to learn if these regions couple with the intermittent region at the relevant frequencies of interest. This is delineated using cross-coherence analysis, which provides a normalized coupling coefficient of the pressure fluctuations between any two locations across the frequency spectrum. Whereas a coherence coefficient ($Coh(f)$) of one corresponds to a linear coupling between the given location and the reference location at that particular frequency, $Coh(f)$ of zero corresponds to no coupling at that frequency. Figure 11 shows the cross-coherence spectra along the streamwise direction for the baseline configuration with the reference location chosen at $x = -8.5\delta$ and $\phi = 0°$. It can be observed that $Coh(f)$ within the incoming boundary layer is quite minor and does not exceed 0.15 across all frequencies. By contrast, the region surrounding the downstream part of the separated flow ($x > -4\delta$), the reattachment region and the relaxing boundary layer exhibit substantial levels of $Coh(f)$. Importantly, $Coh(f)$ exceeding 0.5 can be observed over the Strouhal number range up to 0.05, which is the range corresponding to the low-frequency pulsations of the separation shock foot. This confirms that the pressure fluctuations that occur at the downstream regions of the separated flow and beyond do couple with the separation shock motions at low frequencies and can impact the low-frequency pulsations of the separation shock foot.

3.4.2. *Two-point cross-correlation analysis*

Two-point cross-correlation was obtained over the entire measurement domain to learn how the pressure fluctuations are temporally organized within the SBLI unit with respect to the reference location at the intermittent region ($x = -8.5\delta$ and $\phi = 0°$).
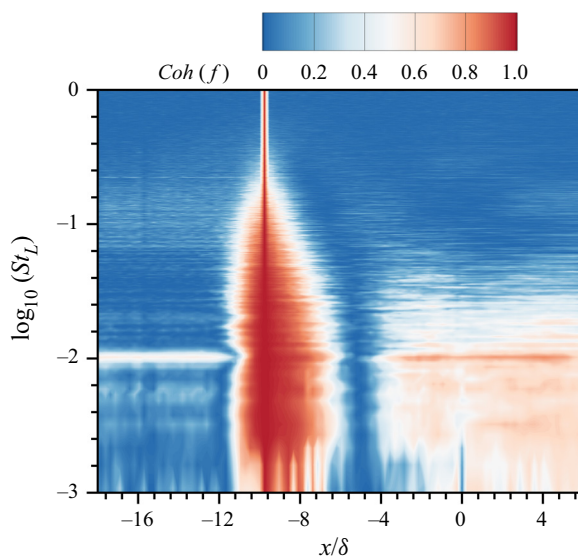
961 A5-22

Figure 11. Streamwise evolution of cross-coherence spectra across the SBLI with the reference location at the intermittent region.

Learning which regions of the SBLI lead and lag the intermittent region provides a building block to uncover the mechanisms that drive the separated shock motion. The results presented are an average 40 randomly sampled data snippets that were 1000 samples (25 ms) long. The uncertainty in the cross-correlation quantified as the 99 % one-sided confidence bound from the 40 sample data snippets is also presented.

Figure 12(*a*) presents the evolution of the two-point cross-correlation along the streamwise direction of the SBLI unit spanning the incoming through relaxing boundary layers. The cross-correlation field at any given time delay is qualitatively identical to the zero delay cross-correlation field (figure 10) in terms of the regions that correlate to greater or lesser extents with the reference location. Figure 12(*b*–*d*) presents the cross-correlations at select locations along $\phi = 0°$ in the form of line plots to provide certain noteworthy details. Beginning with the cross-correlations at the incoming boundary layer presented in figure 12(*b*), it can be observed that spike corresponding to the shock jitter due to the passage of the turbulent structures could not be captured by the PSP technique; this limitation is imposed by the camera exposure time of 25 µs and the inherent attenuation of high frequencies by the paint. With the jitter blocked out, the cross-correlation exhibits two broad negative peaks ($Corr \approx -0.15$), one where the separation shock leads the incoming boundary layer (which is unphysical) and a slightly stronger peak where the separation shock lags the incoming boundary layer by 0.2 ms. Remarkably, the negative correlation persists over 20δ upstream of the separation shock. Further, the correlation peak at $x = -29.5\delta$ exhibits a marginal increase in delay and a slight reduction in the peak negative correlation magnitude compared with $x = -14.3\delta$. A very similar correlation magnitude was also observed in earlier studies with similar separation scales (e.g. Chandola, Huang & Estruch-Samper (2017) in forward-facing step, Priebe & Martín (2012) in compression ramp and Brusniak & Dolling (1994) in blunt fin interactions). Furthermore, Poggie & Porter (2019) demonstrated that the peak correlation between the incoming boundary layer velocity fluctuation and separation shock location occurs several characteristic boundary layer convection times earlier, consistent with the present measurement. The negative
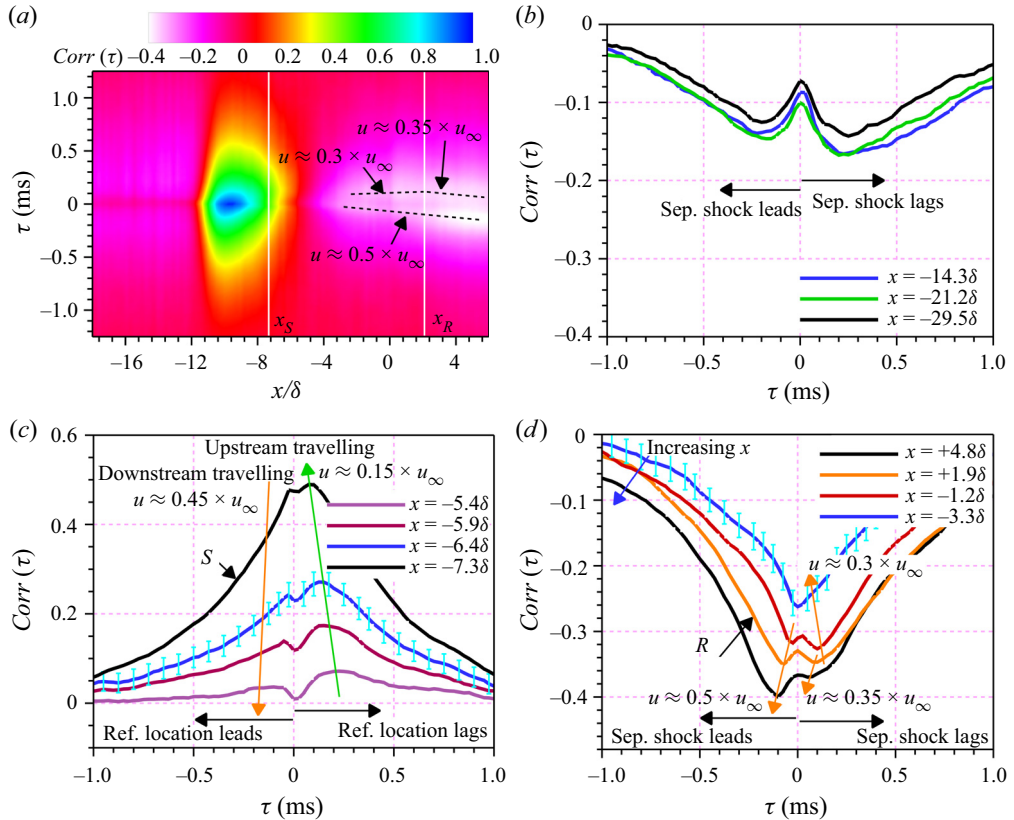
Figure 12. Two-point cross-correlation of different regions within SBLI with reference to the intermittent region. (*a*) Contour of streamwise evolution of the cross-correlation. Selections of cross-correlation plots from representative regions: (*b*) incoming boundary layer, (*c*) intermittent region and (*d*) separated flow, reattachment locus and relaxing boundary layer. Here 'S' and 'R' denote the curves corresponding to the mean separation and reattachment locations that were determined from the surface streakline image of figure 4(*b*). Ref., reference; Sep., separated.

correlation extends over a time scale greater than 1 ms (see figure 12*b*), which is similar to the separation shock low-frequency pulsation frequency range. The significance of these observations in the context of the separation shock pulsations is expounded in § 3.4.3.

We turn our attention to the intermittent region until the mean separation locus where a positive correlation was observed with the intermittent region at zero lag. Figure 12(*c*) shows the occurrence of two positive correlation peaks of similar magnitudes corresponding to the reference location leading and lagging, respectively. Tracking the progression of the time delay of the peaks enables computing the average propagation velocity of the pressure perturbations and their propagation direction. For example, the peaks corresponding to the positive time delay ('reference location lags') occur at increased delay with downstream distance, which shows that this corresponds to an upstream-propagating perturbation; the corresponding propagation velocity is determined to be $\approx 0.15 \times u_\infty$ ($= 90 \text{ m s}^{-1}$). Earlier works by Gonsalez & Dolling (1993) and others used a boxcar approach that tracked the pressure fluctuations above a threshold within the intermittent region over multiple transducers to compute separation shock foot velocity. The cross-correlation is essentially a similar approach that takes both positive and negative pressure fluctuations at the limit of zero threshold. The propagation

961 A5-24

Branch location	Propagation direction	Upper bound	Lower bound
Intermittent region	Upstream	112 m s^{-1}	74 m s^{-1}
Intermittent region	Downstream	518 m s^{-1}	172 m s^{-1}
Reattachment region	Upstream	242 m s^{-1}	145 m s^{-1}
Reattachment region	Downstream	406 m s^{-1}	135 m s^{-1}
Separated flow	Downstream	378 m s^{-1}	227 m s^{-1}

Table 4. Bounds of the propagation velocity of the various pressure perturbation branches identified.

velocity from the cross-correlation analysis is substantially higher than the separation shock foot velocity of $(0.02–0.05) \times u_\infty$ reported in the literature (Gonsalez & Dolling 1993; Clemens & Narayanaswamy 2014). Furthermore, the propagation velocity from the cross-correlation analysis is also higher than the shock velocity obtained in § 3.3.1 based on the intermittent region and characteristic separation shock time scale $(0.015 \times u_\infty)$. The peak corresponding to the negative time delay ('reference location leads') is determined to propagate downstream at an average velocity of $0.45 \times u_\infty$ (≈ 260 m s^{-1}), once again being substantially greater than the shock propagation velocity.

Next, examining the downstream regions of the separated flow, the reattachment region and the downstream relaxing boundary layer (figure 12d), two distinct negative correlation peaks are observed, corresponding to the positive and negative time delays with respect to the separation shock. Figure 12(d) shows that the positive time delay branch (separation shock lags) has a negative peak at a maximum delay of 0.125 ms, which occurs in the reattachment region. Both upstream- and downstream-propagating disturbances can be observed to originate at this location and the propagation velocity was determined to be approximately $0.3 \times u_\infty$ (≈ 180 m s^{-1}) for upstream and $0.35 \times u_\infty$ (≈ 203 m s^{-1}) for downstream directions. The trajectory of the upstream-propagating branch was further tracked in figure 12(a) and was found to terminate just downstream of the shear layer initial growth region. Figure 12(a) also shows that the perturbations corresponding to the negative time delay branch (separation shock leads) originates just downstream of the shear layer initial growth region and propagates downstream through the separated flow and into the relaxing boundary layer as observed from the white contour marked with a black dashed line in figure 12(a). Once again, the downstream disturbance propagates at a velocity of $\approx 0.5 \times u_\infty$ (≈ 280 m s^{-1}) and the velocity is nearly constant along the separated flow and downstream, as discerned from the linear evolution of the peak time delay with distance of the negative time delay branch (black dashed line). The mechanisms that generate the different perturbations and the causes for the divergence in the propagation velocity discussed earlier are presented in § 4.

Before progressing to the next section, it is important to comment on the uncertainty in the propagation velocity of the various pressure perturbations. The main cause of uncertainty is the time discretization of 0.025 ms between the successive pressure fields. Because of the limited size of the SBLI unit, the greatest time lag between the correlation peaks of different locations is only a modest multiple of the time discretization. Furthermore, different entities within the SBLI unit offer different spatial extents from which to compute the velocities, which forms another contributing factor of the uncertainty. Hence, an estimate of the error bounds of the propagation velocity was obtained by considering the peak time lag shifted up and down by the time discretization. The resulting values are presented in table 4.

3.4.3. *Conditionally averaged pressure field sequence*

The analysis performed so far delineated the various regions within the SBLI that are linearly coupled to the separation shock oscillations, as well as the different upstream- and downstream-propagating disturbances that lead and lag the separation shock motions. While these are indeed key insights that are examined further, important shortcomings of this analysis are that: (1) the flow processes within the SBLI are nonlinear that can cause potential deviations in the observations based on the linear analysis and (2) the analysis provides insufficient physical description of the mechanisms that drive the separation bubble pulsations. In this section, the pressure fluctuation fields within the SBLI unit that precede and succeed the separation shock motions are presented in detail to shed light on the nonlinear effects of the interactions as well as the mechanisms that drive the separation shock motion.

The fundamental challenge with analysing the bulk separation shock motions is that the separation bubble pulsations are broadband and are a superposition of different modes of oscillations as demonstrated by Adler & Gaitonde (2018) and Priebe & Martín (2012), among others. The bulk separation shock motion is often overlapped with local rippling caused by boundary layer structures and it is hard to distinguish if the discerned separation shock motion is due to the local rippling or a global pulsation. While many approaches are possible for studying the bulk separation shock motions, such as tracking the spanwise-average iso-pressure (e.g. Wu & Martin 2008), the strategy presented here exploits the fact that the separation shock pressure fluctuations at a given location have strong azimuthal correlation. As a result, when a large number of pressure fields are conditionally averaged based on the local pressure fluctuation threshold, the conditional averaged quantity will iron out the spanwise ripples and reveal the bulk correlated pressure fluctuations across the azimuth. The implementation of this strategy leverages the large amount of data samples available from the experiments to downselect the instances of bulk separation shock motion that extends over a long duration while collecting adequate numbers of pressure field samples for converged results. The following describes the strategy employed.

The overall goal of the strategy is to isolate the positive and negative pressure excursion events in the intermittent region (interpreted as separation shock motions) and observe the conditionally averaged sequence of pressure fluctuation fields within the entire SBLI preceding and succeeding the pressure excursion over a time period corresponding to the peak separation shock pulsation frequency. The key requirement of the chosen instances to build the conditional average is that there should be no pressure fluctuations of the opposite sign in the intermittent region which can corrupt the statistical process over the interrogation duration. To this end, the entire pressure field sequence was low-pass-filtered with 2 kHz cut-off to remove the frequency content that substantially exceeds the low-frequency pulsations of the separation bubble. A reference region within the intermittent region was chosen as an average over a 2.4 mm × 2.4 mm region, and the maxima or minima in the pressure fluctuations at the reference location were identified. Next, those maxima (minima) with positive (negative) pressure fluctuations that were separated from the preceding neighbour by more than a threshold of 2.5 ms were identified and downselected (annotated as '*B*' and '*A*' in figure 13). This downselection ensures that only one minimum (maximum) occurs between '*A*' and '*B*' (denoted as M_{AB} in figure 13) and M_{AB} is separated from the nearest positive (negative) pressure fluctuation by a reasonably long period of time. On an average, the nearest preceding and succeeding zero crossing of pressure fluctuation in the reference location was separated by approximately
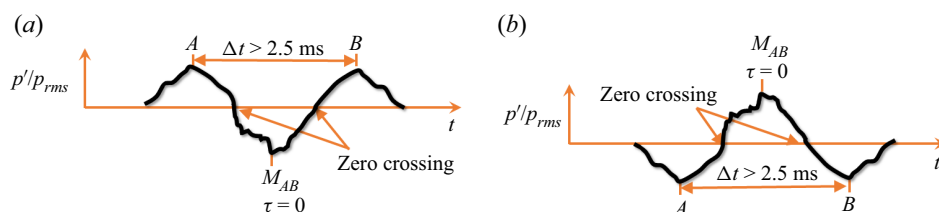
Figure 13. Schematic illustration of the relative temporal layout of the surrounding peaks '*A*' and '*B*' in relation to the local maxima/minima 'M_{AB}' that is referenced as $\tau = 0$ for the conditional averaging of the pressure field time sequence.

1.5 ms from M_{AB}. Overall, approximately 900 individual realizations of maxima (and minima) were collected from more than 10 000 identified maxima (and minima) spanning four test runs. The run-to-run variations in the sequence were minimal and did not interfere with the results. The time instances of M_{AB} were set as a reference time $\tau = 0$ and a sequence of conditionally averaged pressure fluctuation fields was obtained between $\tau = \pm 1.2$ ms referenced to $\tau = 0$. The pressure fluctuation fields were normalized by their local p_{rms} to emphasize the relative excursion to the r.m.s. value, which made a more equitable representation of both low-p_{rms} and high-p_{rms} regions within the SBLI. It should be noted the low-pass filtering at 2 kHz did not impact the overall conditional averaging sequence.

Figure 14(*a*) presents the time sequence of p'/p_{rms} at specific locations of interest and figure 14(*b–e*) shows a sequence of conditional average p'/p_{rms} fields at different time delays corresponding to a positive pressure fluctuation in the intermittent region (separation shock moving upstream of its mean location). Supplementary movie 2 provides the sequence from which figure 14(*b–e*) was extracted. Figure 14(*a*) shows that p'/p_{rms} even at $\tau = -2$ ms exhibits a mild positive pressure value in the intermittent region of $+0.1$, which suggests that the pressure excursion of the intermittent region begins appreciably earlier than the instance of its peak. Correspondingly, the incoming boundary layer (measured -2δ upstream of the intermittent region) and regions within the separated flow exhibit a modest negative p'/p_{rms} at this time instant, as shown in figure 14(*b*) for $\tau = -0.45$ ms. Between about $\tau = -2$ ms and $\tau = -0.3$ ms, there is a strong decrease in p'/p_{rms} within the incoming boundary layer, as observed from figure 14(*a*), to reach a minimum of $p'/p_{rms} = -0.5$ at $\tau = -0.3$ ms. Figure 14(*c*), corresponding to $\tau = -0.35$ ms, shows that there is a groundswell of negative p'/p_{rms} (purple contour) over the entire incoming boundary layer region within the measurement domain that extended over -12δ upstream of the intermittent region and across the entire span of the test article. The corresponding p'/p_{rms} in the intermittent region in this duration increased steadily to 0.7. The p'/p_{rms} within the downstream regions of the separated flow and the reattachment region decreased to -0.5, which did not correspond to a minimum. Interestingly, the slope of p'/p_{rms} curves in the downstream region is nearly identical to that of the incoming boundary layer, as seen in both figures 14(*a*) and 14(*f*). A closer inspection of figure 14(*b*) reveals an earlier onset of the negative pressure fluctuation in the reattachment region compared to upstream locations within the separated flow, as observed from a pale blue contour of negative pressure fluctuation that extends from the mean reattachment location and into the downstream relaxing boundary layer. This negative pressure fluctuation region can also be seen to spread into the separated flow upstream of the ramp leading edge by $\tau = -0.35$ ms (figure 14*c*). Subsequently, whereas the reattachment location has started a steep decline in its pressure fluctuations starting at $\tau = -0.5$ ms, the location just upstream

of the ramp leading edge (blue curve in figure 14*a*) has started to exhibit a steep decline in the pressure fluctuations a little earlier at $\tau = -0.4$ ms.

During -0.3 ms $< \tau \leqslant 0$ ms (instant of peak p'/p_{rms} of the intermittent region), figure 14(*a*) shows that the boundary layer p'/p_{rms} approaches zero across the entire measurement domain. Concomitantly, there is a continued decrease of p'/p_{rms} in the reattachment region and reaches a minimum at $\tau = -0.05$ ms, as shown in figure 14(*a*) (and also figure 14*f*). Within the separated flow, p'/p_{rms} sharply decreases during this time period to reach a minimum value. Figure 14(*a*) shows that p'/p_{rms} within the separated flow just upstream of the ramp leading edge $x = -0.6\delta$ reaches its minimum at $\tau = -0.075$ ms, which is slightly earlier than that of the reattachment location; our limited time resolution ($\Delta \tau = 0.025$ ms) does not allow a better accuracy on the instant of the minimum. Interestingly, the minima of p'/p_{rms} attain very similar values (≈ 1) at both locations close to ramp leading edge and reattachment. Correspondingly, p'/p_{rms} of the intermittent region sharply increases and reaches its maxima exceeding 1.7 at $\tau = 0$ ms. This rapid increase in p'/p_{rms} evidences that sharp bursts of pressure fluctuations occur in the intermittent region on a considerably shorter time scale when compared with the low-frequency unsteadiness. These bursts of pressure fluctuations are responsible for the high value of upstream-propagating perturbation velocities observed in the two-point correlation analysis of § 3.4.2. The swift motions of the separation shock are also consistent with the observations of Priebe & Martín (2012) who demonstrated the growth/burst cycle of the separation bubble that accompanies these motions. The underlying mechanism behind the bursts of separation shock pressure excursion is further expounded in § 4.1.

Supplementary movie 2 also shows that the negative p'/p_{rms} contour moves upstream within the separation bubble and engulfs a large azimuthal region within the separated flow during -0.3 ms $< \tau \leqslant 0$ ms. This strong increase in the size of the negative p'/p_{rms} region in the separation bubble can be observed in figure 14(*d*) obtained at $\tau = 0$ ms. The propagation speed of the upstream edge of negative p'/p_{rms} over this duration was determined by tracking different negative p'/p_{rms} iso-contours, the values standing at $(0.3–0.5) \times u_\infty$. The value range is very similar to the value of $0.45 \times u_\infty$ obtained for the upstream-propagating perturbation within the separated flow in the cross-correlation analysis.

Beyond $\tau = 0$ ms, the intermittent region p'/p_{rms} shows an initially rapid and subsequently a gentler decay. The incoming boundary layer p'/p_{rms} gradually approaches zero at $\tau = 1$ ms and stabilizes around this value. Concomitantly, the pressure fluctuations in the separation bubble and the reattachment region show a steady decay towards zero. Supplementary movie 2 shows that the p'/p_{rms} decay first began within the separation bubble and occurred slightly earlier than $\tau = 0$ ms (at $\tau = -0.075$ ms). The p'/p_{rms} decay onset in the downstream locations such as the reattachment region and relaxing boundary layer occurs at progressively later times than $\tau = -0.075$ ms. This can be observed in figure 14(*e*), where appreciably negative p'/p_{rms} occurs only in the reattachment region and the relaxing boundary layer. This progression of the onset of p'/p_{rms} decay was seen as a downstream-propagating perturbation in the cross-correlation positive time delay branch (figure 12*a*). Notably, whereas the cross-correlation delays showed that the separation shock leads the fluctuations, the actual origin of the perturbation was also located in the upstream vicinity of the separation bubble. Furthermore, the downstream propagation velocity of the p'/p_{rms} front corresponded very closely with the downstream propagation velocity obtained from the cross-correlation analysis.

The azimuthal coverage of the p'/p_{rms} elevations and depressions within the SBLI paints an interesting picture of the underlying dynamics. Figure 14(*b–e*) shows that positive
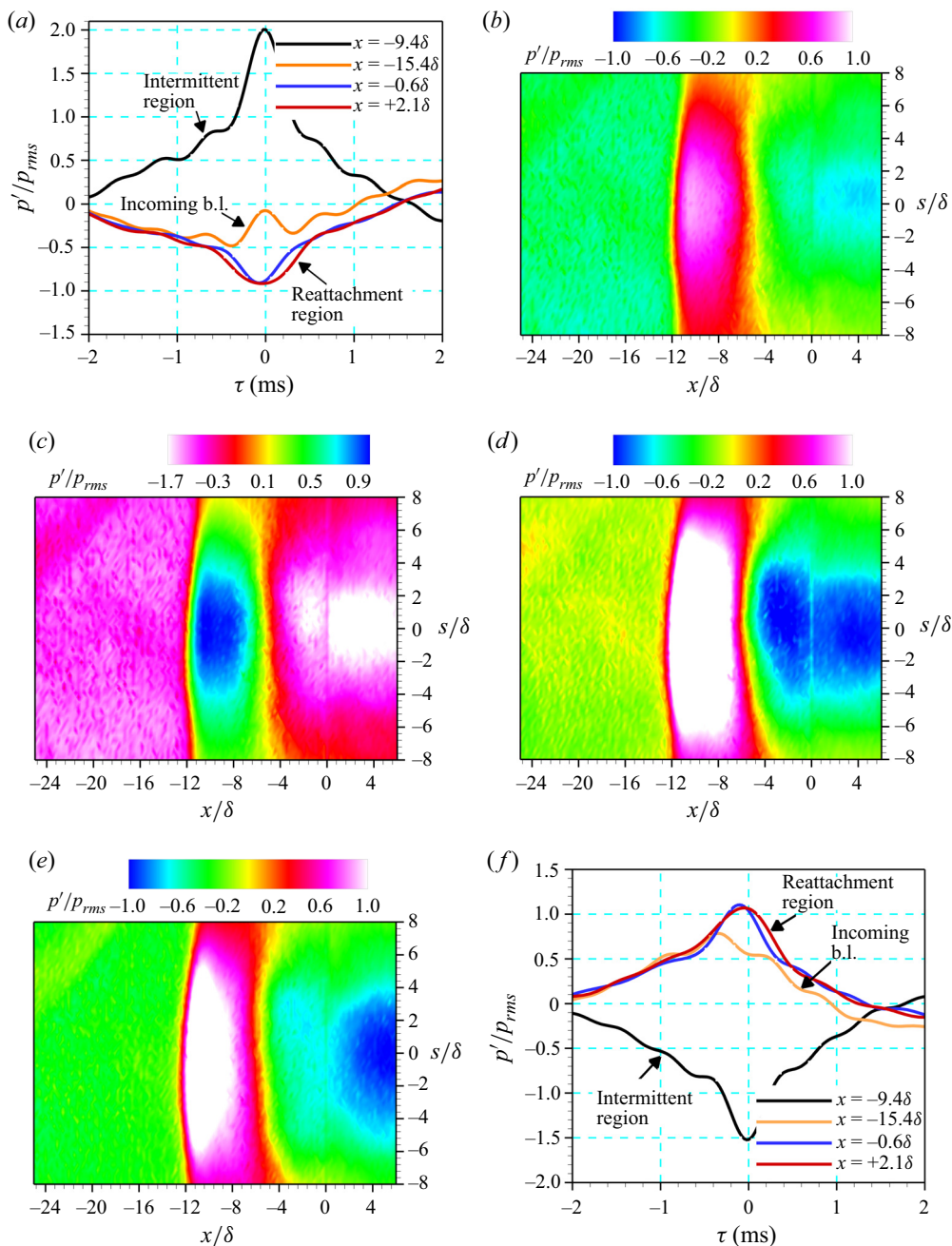
Figure 14. Time sequence of the conditionally averaged p'/p_{rms} fields at various instants of separation shock motions. (*a*) Line plots of p'/p_{rms} sampled at specific locations of interest corresponding to positive p'/p_{rms} in the intermittent region. Corresponding two-dimensional contours of p'/p_{rms} within the SBLI region at specific instances of time with respect to peak of p'/p_{rms} in the intermittent region: (*b*) $\tau = -0.45$ ms, (*c*) $\tau = -0.35$ ms, (*d*) $\tau = 0.0$ ms and (*e*) $\tau = +0.2$ ms. (*f*) Line plots of p'/p_{rms} sampled at specific locations of interest corresponding to negative p'/p_{rms} in the intermittent region. b.l., boundary layer.

p'/p_{rms} within the intermittent region spreads over the entire azimuthal region (visualized from red contour corresponding to zero) and the elevated values of p'/p_{rms} (exceeding 50 % of peak p'/p_{rms} at a given instance) were maintained over a substantial azimuthal region ($-6\delta < s < +6\delta$) surrounding the reference location ($s = 0$). This shows that the conditional average sequence indeed captured the bulk separation shock motion rather than the spanwise undulations. The corresponding azimuthal spread of negative p'/p_{rms} within the separated/reattachment region is much more restricted compared with the intermittent region to within ($-3\delta < s < +3\delta$). Upon closer inspection of the intermittent region p'/p_{rms} in figure 14(*b,c*), it can observed that this azimuthal region ($-2\delta < s < +2\delta$) also exhibits very high values of p'/p_{rms} in the intermittent region. These observations reveal a few important details of the separation shock motions. First, the negative p'/p_{rms} of the separated flow, which has a rather confined azimuthal extent, impacted a substantially large azimuthal region of the intermittent region. In other words, the separation shock motion at a given azimuthal location is non-trivially impacted by the pressure fluctuations in the separated/reattachment region at other azimuthal locations. Second, for the chosen azimuthal location, the greatest impact from the separated/reattachment region occurs over a limited region. Remarkably, the azimuthal length scale $\pm 2\delta$ that showed the greatest negative p'/p_{rms} in the reattachment region and relaxing boundary layer is very similar to the spacing between the Görtler vortices (Floryan 1991; Grilli *et al.* 2013; Loginov *et al.* 2006). This observation along with the elongated nature of the pressure fluctuations in figure 9(*b–e*) and the fact that these p'/p_{rms} streaks are observed earlier than a strong separation shock motion lend support to the postulate of Priebe *et al.* (2016) and Grilli *et al.* (2013) that the Görtler vortices may be an important entity in driving the separation shock motions. The corresponding sequence of negative p'/p_{rms} in the intermittent region shown in figure 14(*f*) is a mirror image of the positive p'/p_{rms} situation presented.

4. Discussion

The conditionally averaged sequence and cross-correlation maps clearly illustrated the azimuthal spread of the pressure fluctuations at different time delays and the importance of making two-dimensional pressure field imaging that is otherwise not possible using point measurements with pressure transducers. The availability of two-dimensional datasets also helps highlight the consonances and differences of the present study compared with earlier high-fidelity computational fluid dynamics and experimental works. First, the preponderance of the streamwise-elongated pressure fluctuations downstream of the ramp leading edge (which likely originate from Görtler vortices) during the pressure excursions of the intermittent region and the azimuthally distanced impact of these streamwise-elongated pressure fluctuations on the separation shock motions emphasize the importance of having adequate spanwise extent of the investigating domain as well as accounting for the Görtler vortices in computational fluid dynamics as stated by Loginov *et al.* (2006), Priebe *et al.* (2016) and Grilli *et al.* (2013), among others. The observation of the azimuthally distanced influence of the separated flow on the separation shock motion was also reported in Pasquariello *et al.* (2017) where their supplementary movies showed that the local undulations in the reattachment line were felt across the span of the separation shock. Pasquariello *et al.* (2017) also observed that the elongated streaks of skin friction coefficient (C_f) elevations due to the Görtler vortices occurred locally in isolation and without any periodicity, which is in strong agreement with the present work. Furthermore, the authors noted that the positive C_f excursion caused the reattachment region moving the reattachment line (reattachment shock) upstream and the separation

shock downstream. Extrapolating from their results, upstream motion of the reattachment shock results in a positive pressure fluctuation in the relaxing boundary layer and elicits a negative pressure response in the intermittent region, which is also consistent with the present work.

The overall characteristics of the PSD evolution within the entire SBLI agreed quite well with those from forward-facing step SBLI (Estruch-Samper & Chandola 2018), impinging SBLI (Agostini, Larchevêque & Dupont 2015) and compression ramp SBLI (Wu & Martin 2008) configurations reported in the literature. As mentioned in § 3.3.1, the point of difference in the PSD evolution between the present study and Estruch-Samper & Chandola (2018) is the occurrence of a PSD hump at $St_L \approx 0.2$–0.4 just downstream of the compression corner that was substantially below the centre frequency of the shear layer observed in the present work. Notably, a similar PSD hump was also reported in other impinging and compression ramp SBLIs (e.g. Agostini *et al.* 2015), suggesting that this is possibly caused by the streamline curvature in the vicinity of the reattachment region of these SBLI units.

The two-point correlation analysis of Wu & Martin (2008) showed that the reattachment line always led the separation line. Both Estruch-Samper & Chandola (2018) and the present study agreed with Wu & Martin (2008) but also evidenced another cross-correlation branch where the separation shock led the reattachment region pressure fluctuations. The present study provided greater details of this branch where it was shown that the true origin of this branch is the events that occur within the separated flow that impacted both the separation shock motions and the downstream pressure perturbations. This observation is in disagreement with Estruch-Samper & Chandola (2018), wherein the authors suggested that the perturbations in the separation shock first impacted the reattachment region and subsequently propagated upstream within the separation bubble. The cause for this divergence is discussed in more detail in § 4.1. Finally, the mean propagation speed of the pressure perturbations within the separation bubble was in the range $(0.4$–$0.5) \times u_\infty$, which is also in agreement with the experimental works of Estruch-Samper & Chandola (2018).

A delayed peak correlation with the incoming boundary layer velocity fluctuations at a time scale that substantially exceeds the flow convection time was observed in Poggie & Porter (2019) whose separation scale was very similar to that of the present work. This is consistent with the delayed correlation in the pressure fluctuation signals of the present work. Interestingly, the velocity correlations in Poggie & Porter (2019) (and mass flux of Wu & Martin (2008)) are presented as spanwise-average quantities, which evidences an overall elevation in the inflow near-wall momentum flux. The present work experimentally supports (albeit indirectly) that the overall inflow momentum excursions occur along the entire spanwise/streamwise domain. Unfortunately, further information about the reattachment line modulation from the incoming boundary layer velocity is not available in Poggie & Porter (2019). Similarly, a broad negative correlation over time scales similar to the separation shock pulsations observed in the present study has also been previously reported in Brusniak & Dolling (1994) in blunt fin interactions of similar separation size. Once again, correlations of the pressure fluctuations at the reattachment location are not available.

In addition to making comparisons with other works, the present study provided a significant experimental support to many of the conjectures by Hu *et al.* (2021) and provided greater insights into how the feedback cycle between the incoming boundary layer fluctuations, shear layer entrainment and reattachment shock motions drives the separation bubble dynamics. First, the present study supports both the downstream

enlargement of the shear layer eddies as well as their reorganization near the reattachment region, based on the examination of the wall pressure PSD. To study the coupling that occurs within the SBLI unit, the present work took an alternative conditional averaging approach that differed from the dynamic mode decomposition approach used by Priebe *et al.* (2016), Hu *et al.* (2021) and Pasquariello *et al.* (2017), which pivots around a specific representative frequency. In the present study, an overall average motion over the time scale that encompassed the low-frequency unsteadiness of the separation bubble was considered. The ensuing temporal sequence of the conditionally averaged pressure fluctuations showed that there is a large-area groundswell of pressure fluctuations in the incoming boundary layer that precedes the separation bubble dynamics. While such a spatially large-scale effect could be present in other units, they were not documented earlier. The presence of such large-scale pressure fluctuation does not contradict but rather elevates the observations of local correlations between the state of the boundary layer and the separation reported by Erengil & Dolling (1991*b*) and Baidya *et al.* (2020), among others. Second, the present work also enhances the current understanding of observed zero-lag correlation and delayed correlation between the incoming boundary layer thickness and the separation shock location that were reported by Baidya *et al.* (2020) and Poggie & Porter (2019). While Baidya *et al.* (2020) focused mainly on the dynamics of the separation shock, the present study and many others (e.g. Dussauge & Piponniau 2008; Priebe *et al.* 2016; Pasquariello *et al.* 2017; Estruch-Samper & Chandola 2018) emphasized the central role of the reattachment region dynamics towards the separation shock motions. The present work showed the sequence of events that painted a picture of how the undulations in the incoming pressure fluctuations impact the reattachment region, and subsequently the separation shock motions. This enhanced description of the underlying dynamics elucidated the cause of both instantaneous and delayed correlation between the boundary layer fluctuations and the separation shock motions. Third, while Pasquariello *et al.* (2017) showed that a larger spanwise extent in the separation shock is influenced by the spanwise wrinkling of the reattachment region, the present work provided greater details of how such a wider spanwise spread occurs in the separation shock motions, the time scales associated with the spanwise coupling, the regions that precede and succeed the reattachment region pressure fluctuations and the overall mechanisms that ultimately cause the observed spanwise coupling. This was shown in the time-resolved conditionally averaged pressure fluctuation sequence and associated discussions.

4.1. *Mechanisms driving the separation bubble pulsations*

Overall, an excellent agreement was observed between the findings of the pressure dynamics and correlations between the present study and the literature. These findings from the conditional average sequence of figure 14 are interpreted to delineate the underlying mechanism that governs the separation bubble pulsations. Before the mechanism is postulated, it is important to comment on the possible links between the pressure fluctuations within the incoming boundary layer and the parameters that relate to the boundary layer properties. It is known that the surface pressure fluctuations beneath the turbulent boundary layers are related to the velocity fluctuations within the boundary layer by the Poisson equation (Bull 1996). Farabee & Casarella (1991) proposed that $p_{rms} = \tau_w \times f(Re_\delta)$ for incompressible boundary layers, wherein the relation to the boundary layer Reynolds number is rather weak. In other words, $p_{rms} \sim \tau_w$ to first order. Other research works (Goody & Simpson 2000; Naka *et al.* 2015) present more intricate details into mapping the pressure fluctuation contributions from various regions within

the boundary layer and turbulent process. In the present work, it is hypothesized that this link between the pressure fluctuations and the streamwise velocity fluctuations occurs in compressible boundary layers employed in the present study. Support for this hypothesis comes from Beresh *et al.* (2013) who observed streamwise-elongated pressure fluctuation structures in their wall pressure trace similar to the large-scale coherent motions within a Mach 2 boundary layer. Similarly, Buchmann *et al.* (2015) observed a long streamwise length scale ($O(5\delta)$) correlation between the pressure and velocity fluctuations in transonic boundary layers.

Figure 14(a,f) shows that the slopes of p'/p_{rms} with time between the incoming boundary layer, the reattachment region and the (sign-flipped) intermittent region are nearly identical until $\tau \approx -0.4$ ms. In other words, as long as the pressure fluctuations in the reattachment region track the incoming boundary layer pressure fluctuations, the intermittent region pressure fluctuations also track the boundary layer pressure fluctuations. Given that the negative pressure fluctuations of the reattachment region correspond to reattachment shock positioned downstream of the mean location and the positive pressure fluctuations of the intermittent region correspond to the separation shock positioned upstream of the mean location, figure 14(a) shows a gradual enlargement of the separation bubble until $\tau \approx -0.4$ ms. Beresh *et al.* (2002) and Ganapathisubramani *et al.* (2009) showed that the enlargement of the separation bubble is accompanied by negative velocity fluctuations in the near-wall region of the boundary layer and a lower incoming boundary layer momentum (Baidya *et al.* 2020). Juxtaposing these observations with figure 14(a) that shows the separation bubble expansion is accompanied by negative surface pressure fluctuations in the incoming boundary layer, we posit that the surface pressure fluctuations of the present boundary layer should be broadly related to both the velocity fluctuations within the boundary layer as well as the overall incoming boundary layer momentum.

Na & Moin (1998) investigated the incompressible separation bubble and showed that the near-wall streaks of the incoming boundary layer populated the shear layer over the separation bubble. Furthermore, Narayanaswamy, Raja & Clemens (2012) tracked the propagation of the near-wall perturbation introduced in the form of a plasma discharge in a Mach 3 SBLI and demonstrated that the discharge-laden structures propagated over the shear layer. Now, following Papamoschou & Roshko (1988), the growth rate of the eddies in the shear layer is determined by the convective Mach number, density ratio (r) and velocity ratio across the shear layer (s):

$$\delta' \sim \Phi(M_C) \times g(r, s). \tag{4.1}$$

Piponniau *et al.* (2009) showed that the contribution from the typical density and velocity ratios across the shear layer ($g(r, s)$) in a SBLI unit makes only a very modest contribution to the entrainment. Furthermore, the average downstream propagation velocity of the pressure perturbations in the cross-correlation analysis ($\approx 0.35 \times u_\infty$) is interpreted as the propagation speed of the coherent eddies in the shear layer following Estruch-Samper & Chandola (2018). From the measured plateau pressure, the bulk inviscid velocity downstream over the shear layer was calculated to be 500 m s^{-1}. These two values provided an estimate of the characteristic reversed flow velocity within the separation bubble as -36 m s^{-1}. Using these estimates, the convective Mach number, $M_C = \Delta U/(a_1 + a_2)$, was estimated to be 1.05. The function $\Phi(M_C)$, presented in Piponniau *et al.* (2009), shows a decreasing trend with M_C until about $M_C \approx 1.3$, above which it plateaus to a constant value. Thus, a negative velocity fluctuation (discerned as a negative pressure fluctuation) in the incoming boundary layer causes an increase in the eddy growth
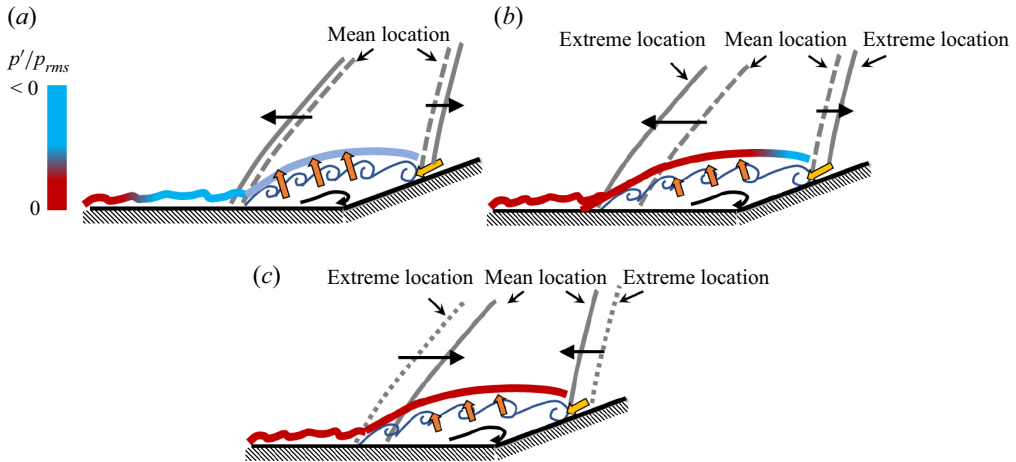
Figure 15. Illustration of the mechanisms that drive the different phases of separation bubble motion: (*a*) gradual expansion, (*b*) rapid expansion and (*c*) relaxation to mean separation size.

rate along the shear layer, which in turn increases the fluid injection at the reattachment region and ultimately causes the separation bubble to expand. While making this argument, we invoke the proposition made by Piponniau *et al.* (2009) that the mass entrainment usually only occurs in the rear half of the separation bubble. The corresponding process is illustrated in figure 15(*a*).

At $\tau \approx -0.35$ ms, figure 14 shows that the boundary layer pressure (and conjecturally the velocity) fluctuations reached a negative peak and began to approach zero. However, it takes about 0.2 ms for the shear layer structures that originate at the separation bubble leading edge to reach the reattachment region, based on the estimated velocity of the shear layer eddies. We posit that this is the cause of a lag of 0.3 ms observed in figure 14(*a*,*f*) between the peak in p'/p_{rms} of the incoming boundary layer and the reattachment region. This process is illustrated in figure 15(*b*). During the propagation time of the 'less negative' pressure (and conjecturally the velocity) streaks through the shear layer, the reattachment region continues to inject mass at a greater rate into the separated flow while the fluid rejected by the shear layer decreases. This can be observed by the continued increase in p'/p_{rms} of the reattachment region without any appreciable change in the slope of the curve until a lag of 0.3 ms, i.e. $\tau = -0.05$ ms in figure 14(*a*,*f*). The greater mass injection rate exacerbates the mass imbalance in the separation bubble and the highest imbalance occurs at the instance the modified streaks reach the reattachment region.

In response to the mass imbalance, the separation bubble rapidly expands in the range -0.35 ms $\leqslant \tau \leqslant -0.1$ ms. This expansion triggers a sharp upstream motion of the separation shock in the range -0.35 ms $\leqslant \tau \leqslant 0$ ms. This process is also illustrated in figure 15(*b*). The rapid expansion of the separation bubble may spur strong events within the separation bubble such as vortex bursting as reported by Priebe & Martín (2012). We posit perhaps some such strong event occurs near the peak instant of p'/p_{rms} in the separation bubble and this peak is first measured just upstream of the ramp leading edge, suggesting the event possibly originated at this location. Based on the measured upstream propagation velocity of the perturbations from the cross-correlation analysis, it takes about 0.1 ms for the perturbations that originate from the strong events near the ramp leading edge to reach the separation shock and trigger a corresponding rapid downstream motion of the separation shock during 0 ms $\leqslant \tau \leqslant +0.4$ ms. While the separation shock moves

downstream rapidly during $0 \text{ ms} \leqslant \tau \leqslant +0.4 \text{ ms}$, a corresponding upstream motion of the reattachment shock is also initiated; however, the gradual slope of p'/p_{rms} suggests that the upstream motion of the reattachment shock is not as rapid as the separation shock. This process is illustrated in figure 15(*c*). The rapid shrinking of the separation bubble continues until p'/p_{rms} of the reattachment region catches up with the slope of the incoming boundary layer p'/p_{rms}, i.e. near-wall momentum fluctuations and/or the accompanying entrainment modulations.

The two-dimensional fields of the conditionally averaged p'/p_{rms} shown in figure 14(*b–e*) evidence that the entire separated flow exhibits a positive/negative p'/p_{rms} modulation in response to the incoming boundary layer during the large-scale pulsation events. Interestingly, however, the strongest modulation within the separation bubble occurs over an azimuthal region of $-2\delta < s < +2\delta$ surrounding the reference azimuth. Over the duration of intense p'/p_{rms} modulation within the separated flow ($-0.4 \text{ ms} \leqslant \tau \leqslant 0 \text{ ms}$), the conditionally averaged p'/p_{rms} sequence shows rapid azimuthally outward spreading of p'/p_{rms} over $-4\delta < s < +4\delta$ within the separation bubble, as observed in figure 14(*c,d*). This shows that strong events that occur within the separation bubble spread laterally within the bubble over a finite span. Interestingly, there is a clear demarcation between the regions that are impacted (dark blue contour of figure 14*d*) and not impacted, thereby illustrating a spanwise disparity in the separation bubble response.

Overall, the present study agrees that the separation bubble dynamics is governed by the mass imbalance within the separation bubble, as suggested by Eaton & Johnston (1981), Wu & Martin (2008) and Piponniau *et al.* (2009). This study also conclusively shows that the imbalance is driven strongly by the long-duration near-wall momentum undulations of the incoming boundary layer that occurs over several boundary layer thicknesses in both streamwise and spanwise (azimuthal) directions. The present study also shows that the gradual undulations of the separation bubble are punctuated by short bursts ($\sim 1 \text{ ms}$) of rapid growth and shrinkage of the separation bubble, which appears to originate just upstream of the ramp leading edge. These events, once again, appear to be driven by the exacerbation of the mass imbalance as the incoming boundary layer undergoes a change in its long-duration near-wall momentum undulations towards zero. The observations further suggest that the formation of the streamwise-elongated structures downstream of the ramp leading edge is a consequence of the reorganization of the shear layer vortices as they propagate through a strong curvature in the vicinity of the ramp leading edge. While it is interesting to note that the onset location of the strong events within the separation bubble is very close to the ramp leading edge and the instant of onset occurs in the presence of the streamwise-elongated p'/p_{rms} downstream of the compression ramp, the present study cannot ascertain a causality between these structures in the reattachment region and the strong events in the separation bubble. Finally, the present study shows that a large span of separation shock is driven upstream/downstream during the strong events, even though only a relatively short span within the separated flow exhibits strong pressure undulations. This suggests that the separation shock at a given spanwise location is impacted by the superposition of spanwise variations in the reattachment location.

At this point, it is also important to draw the boundaries of this conclusion and also to address the influence of area constriction on the separation dynamics. It should be noted that the impact of the incoming boundary layer fluctuations on the shear layer entrainment is restricted to convective Mach number $M_C \leqslant 1.3$. Estruch-Samper & Chandola (2018) state that beyond 'an effective threshold $M_C = 1.25$, the shear layer growth remains practically invariant'. In other words, the direct impact of the incoming boundary layer fluctuations on the shear layer entrainment is a low-Mach-number phenomenon; with
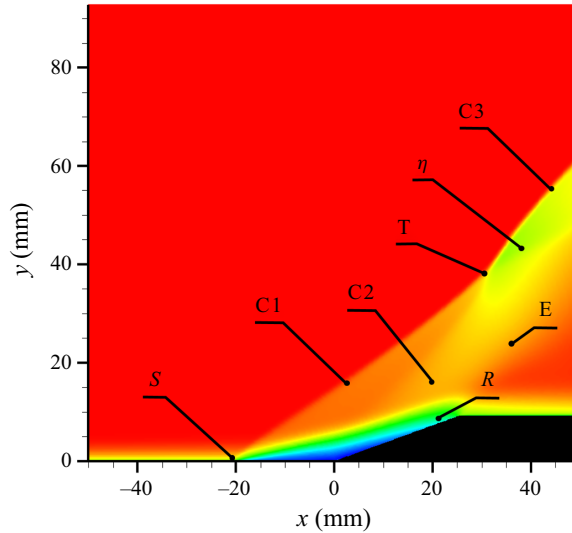
Figure 16. Mean streamwise velocity contour from RANS simulations. The labels include the separation shock (C1), the reattachment shock (C2), the inviscid shock (C3), the triple point of separation and reattachment shock coalescence (T), the expansion fan at the ramp shoulder (E) and the elevated compression region (η).

increasing Mach number, the influence of the incoming boundary layer on the shear layer entrainment would likely reduce. A rule of thumb for the order of magnitude of the low-Mach-number limit for the separation scales presented in this work is possibly between Mach 2.5 and Mach 3.0.

The other point of consideration is the influence of the area constriction on the separation dynamics, i.e. if the flow decelerates rapidly along the SBLI unit that the statistical analysis and the corresponding velocity scaling would become inaccurate. To address this issue, the streamwise velocity field along the centre azimuth from the RANS simulations of Funderburk & Narayanaswamy (2019*a*) is presented in figure 16. The important features that are associated with the SBLI unit are labelled as was done in figure 4(*a*). The evolution of the streamwise velocity shows that its value decreases from the free stream to approximately 500 m s^{-1} in the inviscid region downstream of the separation shock. This velocity value is very consistent with that obtained based on the plateau pressure values presented in § 4.1. The streamwise velocity magnitude in the inviscid region is maintained until downstream of the ramp face until the ramp shoulder and only a modest reduction down to ≈480 m s^{-1} was observed at the ramp shoulder. These values show that the flow deceleration due to the area constriction is modest until well downstream of the reattachment region. Hence, the impact of area constriction on the separation shock dynamics is expected to be modest.

4.1.1. *A note on the presence of Görtler vortices*

There are multiple studies discussed in § 1 that support the central role of the Görtler vortices towards driving the separation bubble dynamics. Thus, it is important to set the perspective of the current work in the context of the earlier related studies.

The presence of the Görtler vortex in the present SBLI unit is certainly open to interpretation because of the absence of the cellular structures in the streakline fields. As pointed out in § 3.3.1, the presence of Görtler vortices is mainly conjectural and indirect

961 A5-36

but supported by calculations and the observations of streamwise-elongated pressure fluctuation streaks downstream of the compression corner. As such, the present study leaves the presence of the Görtler vortices as a strong possibility.

The present work takes the view that emphasizes the role of the mass imbalance within the separation bubble as the driving cause of the separation bubble motions. This mass imbalance is posited to be caused by the local variations in the shear layer entrainment that injects mass at the reattachment region. The mass imbalance mechanism does not require the occurrence of the Görtler vortices in the reattachment region and studies such as that of Baidya *et al.* (2020) were uncertain about the occurrence of the Görtler vortices in their SBLI unit while the low-frequency separation bubble pulsations were still observed. Thus, the Görtler vortices are but a footprint of the state of the shear layer eddies and streamline curvature in the vicinity of the reattachment region. Hence, we posit that the Görtler vortices by themselves may not be the mechanism that drives the SBLI unit. Instead, the Görtler vortices are possibly the outcomes and/or signatures of the driving flow processes that occur within the SBLI unit.

4.1.2. *Role of boundary layers towards driving the separated flow unsteadiness*
Due to the limitations in the signal-to-noise ratio, the measurements reported in the present work cannot identify the streamwise-elongated pressure fluctuation structures within the incoming boundary layer that were earlier observed in Beresh *et al.* (2013). As a result, the present study cannot shed much light into the spanwise rippling of the separation shock. The investigations into the bulk separation shock motions showed that large-scale pressure field undulations within the incoming boundary layer accompanied the separation bubble breathing motions. The undulations in the pressure fluctuations are conjectured to reflect the undulations in the overall incoming boundary layer momentum, which is consistent with McClure (1992) who observed gradual variations in the Pitot pressure over 90 % of the boundary layer thickness during the upstream/downstream separation shock motions. It is remarkable that the Pitot probe was set at a distance $x = -16\delta$, which is similar to the streamwise extent imaged in the present study. While McClure (1992) conducted the Pitot pressure measurements at a discrete streamwise location, the present work shows that the pressure undulations (and possibly the global momentum undulations) occur over a much larger area in both streamwise and spanwise directions. In addition to the gradual separation bubble pulsations, the present study shows that the turnaround of the boundary layer pressure fluctuations towards zero triggers short pulses of rapid separation shock motions. Further, the time sequence of the conditionally averaged pressure fluctuations reveals that the boundary layer fluctuations generate the earliest pressure modulation in the vicinity of the reattachment region. The footprint of the pressure fluctuation field in the reattachment region is elongated along the streamwise direction, which suggests that the boundary layer structures can indeed influence the formation of these streamwise-elongated structures, supporting Hu *et al.* (2021).

5. Conclusions

Two-dimensional high-repetition-rate (40 kHz) surface pressure field imaging was employed to investigate the mechanisms that the drive the shock-induced separation bubble pulsations in light of the recent discoveries that relate to the spanwise flow field organization and the shear layer dynamics. The available experimental measurements on SBLI were almost exclusively performed along fixed spanwise locations that had precluded obtaining a more detailed understanding of the spanwise coupling that occurs within

the SBLI units. Similarly, the spanwise domain size of most high-fidelity computations was less than 5δ (δ is the incoming boundary layer thickness), which limited the ability to unravel the spanwise coupling beyond this spanwise length scale. The present study offset both these limitations and provided a first glimpse of highly resolved pressure field organization within the SBLI unit. The measurement domain extended over 25δ in the spanwise direction and over 25δ along the streamwise directions, which covered a signification portion of the incoming and relaxing boundary layers in addition to the separated flow.

In-house-formulated fast-response PSP was employed for pressure field imaging. The spectral response of the paint was evaluated both theoretically and by direct comparison with high-bandwidth pressure transducers. These evaluations showed that the PSP can capture the dynamic content over at least 10 kHz with less than 50 % attenuation. This response was demonstrated to adequately capture the peak of the separation and reattachment shock pulsations; however, the dominant frequencies within the separation bubble were above the spectral attenuation range of the paint and the camera acquisition rate.

Shock-induced separation was generated by an axisymmetric inward-turning compression ramp, which generated a mean separation length scale, $L_{sep} \approx 10\delta$. While the SBLI unit is fundamentally three-dimensional, the mean surface streakline images and surface pressure fields confirmed that the unit exhibited two-dimensional character over a circumferential region that extended $\pm 6\delta$ about the centre span. The PSD of the pressure fluctuations within the SBLI unit exhibited trends consistent with those of the literature in terms of peak Strouhal number of separation shock pulsations, the relationship between peak Strouhal numbers of separation and reattachment shock pulsations as well as the downward frequency shift of the PSD within the separation bubble along the downstream direction. Interestingly, a band of PSD elevation ($St_L = 0.2$–0.4) occurs abruptly at the ramp leading edge and extended until downstream of the reattachment region. This band was reported earlier in SBLI generated by the compression ramp and impinging shock and not by a forward-facing step, suggesting that this band may have origins in structures generated by strong streamline curvature near the reattachment region. The time sequence of the surface pressure fluctuations revealed the occurrence of streamwise-elongated streaks originated near the ramp leading edge; the concomitant analysis supports that these structures could be the footprints of Görtler vortices and are perhaps responsible for the $St_L = 0.2$–0.4 band.

The cross-correlation fields demonstrated that the pressure fluctuations within the separation shock at a given azimuth are correlated with those within the separated flow and reattachment region over a region of azimuthal distance that spanned $\pm 4\delta$, which demonstrated the spanwise coupling that contributes to the separation shock motions. The correlation fields further demonstrated the occurrence of different pressure perturbations within the separated flow that lead and lag the separation shock motions. Nodes of upstream- and downstream-propagating pressure perturbations were identified in the vicinity of the reattachment region and separated flow. The propagation velocity of the downstream fluctuations agreed very well with the shear layer convection velocity, suggesting these perturbations are driven by the shear layer events.

A time sequence of conditionally averaged pressure fluctuation field that surrounded an instance of isolated maxima and minima in the intermittent-region pressure fluctuation was constructed to provide a physical context to the pressure perturbations. The time sequence revealed the occurrence of global variations in the inflow momentum whose time scales agreed with the separation bubble pulsation time scales. The separation bubble pulsations

responded rather gradually to the mass imbalance caused by the shear layer entrainment, which in turn was preceded by the variations in the global inflow momentum. However, whenever there was a change in the global momentum fluctuations to approach zero, a corresponding sharp response within the separation bubble was triggered due to rapid aggravation of the mass imbalance; this caused a rapid upstream/downstream separation shock motion. These findings support the mass imbalance within the separated flow driven by the shear layer entrainment as being the driving interaction of the separation bubble pulsations. These findings also lend a new lens to the potential causes of the extreme events that occur within the separation bubble that result in rapid separation shock motions. Overall, the present study shows that the bulk separation shock motion is a combination of gradual pulsations punctuated by rapid motions.

Declaration of interests. The authors report no conflict of interest.

Author ORCIDs.
Venkat Narayanaswamy https://orcid.org/0000-0003-1831-6321.

References

ADLER, M.C. & GAITONDE, D.V. 2018 Dynamic linear response of a shock/turbulent-boundary-layer interaction using constrained perturbations. *J. Fluid Mech.* **840**, 291–341.

AGOSTINI, L., LARCHEVÊQUE, L. & DUPONT, P. 2015 Mechanism of shock unsteadiness in separated shock/boundary-layer interactions. *Phys. Fluids* **27** (12), 126103.

ANDREOPOULOS, J. & MUCK, K.C. 1987 Some new aspects of the shock-wave/boundary-layer interaction in compression-ramp flows. *J. Fluid Mech.* **180**, 405–428.

BABINSKY, H. & HARVEY, J.K. 2011 *Shock Wave-Boundary-Layer Interactions*, vol. 32. Cambridge University Press.

BAIDYA, R., SCHARNOWSKI, S., BROSS, M. & KÄHLER, C.J. 2020 Interactions between a shock and turbulent features in a Mach 2 compressible boundary layer. *J. Fluid Mech.* **893**, A15.

BERESH, S.J., CLEMENS, N.T. & DOLLING, D.S. 2002 Relationship between upstream turbulent boundary-layer velocity fluctuations and separation shock unsteadiness. *AIAA J.* **40** (12), 2412–2422.

BERESH, S.J., HENFLING, J.F., SPILLERS, R.W. & PRUETT, B.O.M. 2011 Fluctuating wall pressures measured beneath a supersonic turbulent boundary layer. *Phys. Fluids* **23** (7), 075110.

BERESH, S.J., HENFLING, J.F., SPILLERS, R.W. & PRUETT, B.O.M. 2013 Very-large-scale coherent structures in the wall pressure field beneath a supersonic turbulent boundary layer. *Phys. Fluids* **25** (9), 075110.

BRUSNIAK, L. & DOLLING, D.S. 1994 Physics of unsteady blunt-fin-induced shock wave/turbulent boundary layer interactions. *J. Fluid Mech.* **273**, 375–409.

BUCHMANN, N.A., KÜCÜKOSMAN, Y.C., EHRENFRIED, K. & KÄHLER, C.J. 2015 Wall pressure signature in compressible turbulent boundary layers. In *Progress in Wall Turbulence*, vol. 2, pp. 93–102. Springer.

BULL, M.K. 1996 Wall-pressure fluctuations beneath turbulent boundary layers: some reflections on forty years of research. *J. Sound Vib.* **190** (3), 299–315.

CHANDOLA, G., HUANG, X. & ESTRUCH-SAMPER, D. 2017 Highly separated axisymmetric step shock-wave/turbulent-boundary-layer interaction. *J. Fluid Mech.* **828**, 236–270.

CHERRY, N.J., HILLIER, R. & LATOUR, M.E.M.P. 1984 Unsteady measurements in a separated and reattaching flow. *J. Fluid Mech.* **144**, 13–46.

CLEMENS, N.T. & NARAYANASWAMY, V. 2014 Low-frequency unsteadiness of shock wave/boundary layer interactions. *Annu. Rev. Fluid Mech.* **46**, 469–492.

DESHPANDE, A.S. & POGGIE, J. 2021 Large-scale unsteadiness in a compression ramp flow confined by sidewalls. *Phys. Rev. Fluids* **6** (2), 024610.

DOLLING, D.S. 1993 Fluctuating loads in shock wave/turbulent boundary layer interaction: tutorial and update. In *31st Aerospace Sciences Meeting*, p. 284. AIAA.

DOLLING, D.S. 2001 Fifty years of shock-wave/boundary-layer interaction research: what next? *AIAA J.* **39** (8), 1517–1531.

DUPONT, P., HADDAD, C., ARDISSONE, J.P. & DEBIEVE, J.F. 2005 Space and time organisation of a shock wave/turbulent boundary layer interaction. *Aerosp. Sci. Technol.* **9** (7), 561–572.

DUSSAUGE, J.-P. & PIPONNIAU, S. 2008 Shock/boundary-layer interactions: possible sources of unsteadiness. *J. Fluids Struct.* **24** (8), 1166–1175.

EATON, J.K. & JOHNSTON, J.P. 1981 A review of research on subsonic turbulent flow reattachment. *AIAA J.* **19** (9), 1093–1100.

EGAMI, Y., SATO, Y. & KONISHI, S. 2019 Development of sprayable pressuresensitive paint with a response time of less than 10 µs. *AIAA J.* **57** (5), 2198–2203.

ERENGIL, M.E. & DOLLING, D.S. 1991a Correlation of separation shock motion with pressure fluctuations inthe incoming boundary layer. *AIAA J.* **29** (11), 1868–1877.

ERENGIL, M.E. & DOLLING, D. 1991b Unsteady wave structure near separation in a Mach 5 compression ramp interaction. *AIAA J.* **29**, 728–735.

ESTRUCH-SAMPER, D. & CHANDOLA, G. 2018 Separated shear layer effect on shock-wave/turbulent-boundary-layer interaction unsteadiness. *J. Fluid Mech.* **848**, 154–192.

FARABEE, T.M. & CASARELLA, M.J. 1991 Spectral features of wall pressure fluctuations beneath turbulent boundary layers. *Phys. Fluids* A **3** (10), 2410–2420.

FLORYAN, J.M. 1991 On the Görtler instability of boundary layers. *Prog. Aerosp. Sci.* **28** (3), 235–271.

FUNDERBURK, M.L. & NARAYANASWAMY, V. 2019a Investigation of negative surface curvature effects in an axisymmetric shock boundary layer interaction. *AIAA J* **57** (4), 1594–1607.

FUNDERBURK, M.L. & NARAYANASWAMY, V. 2019b Spectral signal quality of fast pressure sensitive paint measurements in turbulent shock-wave/boundary layer interactions. *Exp. Fluids* **60** (10), 1–20.

GAITONDE, D.V. 2015 Progress in shock wave/boundary layer interactions. *Prog. Aerosp. Sci.* **72**, 80–99.

GANAPATHISUBRAMANI, B., CLEMENS, N.T. & DOLLING, D.S. 2006 Large-scale motions in a supersonic turbulent boundary layer. *J. Fluid Mech.* **556**, 271–282.

GANAPATHISUBRAMANI, B., CLEMENS, N.T. & DOLLING, D.S. 2009 Low-frequency dynamics of shock-induced separation in a compression ramp interaction. *J. Fluid Mech.* **636**, 397–425.

GONSALEZ, J. & DOLLING, D. 1993 Correlation of interaction sweepback effects on unsteady shock-induced turbulent separation. In *31st Aerospace Sciences Meeting*, p. 776. AIAA.

GOODY, M.C. & SIMPSON, R.L. 2000 Surface pressure fluctuations beneath two-and three-dimensional turbulent boundary layers. *AIAA J.* **38** (10), 1822–1831.

GRAMANN, R.A. & DOLLING, D.S. 1990 Detection of turbulent boundary-layer separation using fluctuating wall pressure signals. *AIAA J.* **28** (6), 1052–1056.

GRILLI, M., HICKEL, S. & ADAMS, N.A. 2013 Large-eddy simulation of a supersonic turbulent boundary layer over a compression–expansion ramp. *Intl J. Heat Fluid Flow* **42**, 79–93.

GRILLI, M., SCHMID, P.J., HICKEL, S. & ADAMS, N.A. 2012 Analysis of unsteady behaviour in shockwave turbulent boundary layer interaction. *J. Fluid Mech.* **700**, 16–28.

HU, W., HICKEL, S. & VAN OUDHEUSDEN, B.W. 2021 Low-frequency unsteadiness mechanisms in shock wave/turbulent boundary layer interactions over a backward-facing step. *J. Fluid Mech.* **915**, A107.

HUMBLE, R.A., ELSINGA, G.E., SCARANO, F. & VAN OUDHEUSDEN, B.W. 2009 Three-dimensional instantaneous structure of a shock wave/turbulent boundary layer interaction. *J. Fluid Mech.* **622**, 33–62.

JIAO, L., PENG, D. & LIU, Y. 2018 Dynamic response of polymer ceramic pressure-sensitive paint: improved model considering thickness effect. *AIAA J.* **56** (7), 2903–2906.

KAMEDA, M., SEKI, H., MAKOSHI, T., AMAO, Y. & NAKAKITA, K. 2012 A fast-response pressure sensor based on a dye-adsorbed silica nanoparticle film. *Sensors Actuators* B **171**, 343–349.

KASAI, M., SASAKI, D., NAGATA, T., NONOMURA, T. & ASAI, K. 2021 Frequency response of pressure-sensitive paints under low-pressure conditions. *Sensors* **21** (9), 3187.

KISTLER, A.L. 1959 Fluctuation measurements in a supersonic turbulent boundary layer. *Phys. Fluids* **2** (3), 290–296.

LEONARD, M.D. & NARAYANASWAMY, V. 2021 Investigation of shock dynamics in an axisymmetric inlet/isolator with attached boundary layers. *J. Fluid Mech.* **908**, A42.

LOGINOV, M.S., ADAMS, N.A. & ZHELTOVODOV, A.A. 2006 Large-eddy simulation of shock-wave/ turbulent-boundary-layer interaction. *J. Fluid Mech.* **565**, 135–169.

LOWSON, M.V. 1968 Prediction of boundary layer pressure fluctuations. *Tech. Rep.* Wyle Labs Inc., Huntsville, AL.

LÜDEKE, H., RADESPIEL, R. & SCHÜLEIN, E. 2004 Simulation of streamwise vortices at the flaps of re-entry vehicles. *Aerosp. Sci. Technol.* **8** (8), 703–714.

MCCLURE, W.B. 1992 *An Experimental Study of the Driving Mechanism and Control of the Unsteady Shock-Induced Turbulent Separation in a Mach 5 Compression Corner Flow*. The University of Texas at Austin.

MCMULLEN, R.M., HUYNH, D.P., GREGORY, J. & CRAFTON, J.W. 2013 Dynamic calibrations for fast-response porous polymer/ceramic pressure-sensitive paint. In *AIAA Ground Testing Conference*, p. 3123. AIAA.

NA, Y. & MOIN, P. 1998 Direct numerical simulation of a separated turbulent boundary layer. *J. Fluid Mech.* **374**, 379–405.

NAKA, Y., STANISLAS, M., FOUCAUT, J.-M., COUDERT, S., LAVAL, J.-P. & OBI, S. 2015 Space–time pressure–velocity correlations in a turbulent boundary layer. *J. Fluid Mech.* **771**, 624–675.

NARAYANASWAMY, V., RAJA, L.L. & CLEMENS, N.T. 2012 Control of unsteadiness of a shock wave/turbulent boundary layer interaction by using a pulsed-plasma-jet actuator. *Phys. Fluids* **24** (7), 076101.

PANDEY, A. & GREGORY, J.W. 2016 Frequency-response characteristics of polymer/ceramic pressure-sensitive paint. *AIAA J.* **54** (1), 174–185.

PAPAMOSCHOU, D. & ROSHKO, A. 1988 The compressible turbulent shear layer: an experimental study. *J. Fluid Mech.* **197**, 453–477.

PASQUARIELLO, V., HICKEL, S. & ADAMS, N.A. 2017 Unsteady effects of strong shock-wave/boundary-layer interaction at high Reynolds number. *J. Fluid Mech.* **823**, 617–657.

PIPONNIAU, S., DUSSAUGE, J.-P., DEBIEVE, J.-F. & DUPONT, P. 2009 A simple model for low-frequency unsteadiness in shock-induced separation. *J. Fluid Mech.* **629**, 87–108.

PIROZZOLI, S., GRASSO, F. & GATSKI, T.B. 2004 Direct numerical simulation and analysis of a spatially evolving supersonic turbulent boundary layer at $m = 2.25$. *Phys. Fluids* **16** (3), 530–545.

POGGIE, J. & PORTER, K.M. 2019 Flow structure and unsteadiness in a highly confined shock-wave–boundary-layer interaction. *Phys. Rev. Fluids* **4** (2), 024602.

PRIEBE, S. & MARTÍN, M.P. 2012 Low-frequency unsteadiness in shock wave–turbulent boundary layer interaction. *J. Fluid Mech.* **699**, 1–49.

PRIEBE, S., TU, J.H., ROWLEY, C.W. & MARTÍN, M.P. 2016 Low-frequency dynamics in a shock-induced separated flow. *J. Fluid Mech.* **807**, 441–477.

SCHUELEIN, E. & TROFIMOV, V.M. 2011 Steady longitudinal vortices in supersonic turbulent separated flows. *J. Fluid Mech.* **672**, 451–476.

SMITS, A.J. & DUSSAUGE, J.-P. 2006 *Turbulent Shear Layers in Supersonic Flow*. Springer Science & Business Media.

THOMAS, F.O., PUTNAM, C.M. & CHU, H.C. 1994 On the mechanism of unsteady shock oscillation in shock wave/turbulent boundary layer interactions. *Exp. Fluids* **18** (1), 69–81.

TOUBER, E. & SANDHAM, N.D. 2009 Large-eddy simulation of low-frequency unsteadiness in a turbulent shock-induced separation bubble. *Theor. Comput. Fluid Dyn.* **23** (2), 79–107.

VARIGONDA, S.V. & NARAYANASWAMY, V. 2021 Methodology to image the panel surface pressure power spectra in weakly coupled fluid/structure interactions. *Exp. Fluids* **62** (11), 1–17.

WINSLOW, N.A., CAROLL, B.F. & KURDILA, A.J. 2001 Model development and analysis of the dynamics of pressure-sensitive paints. *AIAA J.* **39** (4), 660–666.

WU, M. & MARTIN, M.P. 2008 Analysis of shock motion in shockwave and turbulent boundary layer interaction using direct numerical simulation data. *J. Fluid Mech.* **594**, 71–83.

ZHELTOVODOV, A. 2006 Some advances in research of shock wave turbulent boundary layer interactions. In *44th AIAA Aerospace Sciences Meeting and Exhibit*, p. 496. AIAA.

ZHUANG, Y., TAN, H.-J., LI, X., SHENG, F.-J. & ZHANG, Y.-C. 2018 Görtler-like vortices in an impinging shock wave/turbulent boundary layer interaction flow. *Phys. Fluids* **30** (6), 061702.